Synergistic radar and radiometer retrievals of ice hydrometeors

Simon Pfreundschuh[1], Patrick Eriksson[1], Stefan A. Buehler[2], Manfred Brath[2], David Duncan[1, 4], Richard Larsson[3], and Robin Ekelund[1]

[1]Department of Space, Earth and Environment, Chalmers University of Technology, 41296 Gothenburg, Sweden
[2]Meteorologisches Institut, Fachbereich Geowissenschaften, Centrum für Erdsystem und Nachhaltigkeitsforschung (CEN), Universität Hamburg, Bundesstraße 55, 20146 Hamburg, Germany
[3]Max Planck Institute for Solar System Research, Justus-von-Liebig-Weg 3, 37077 Göttingen, Germany
[4]Now at European Centre for Medium-Range Weather Forecasts, Shinfield Park, Reading RG2 9AX, United Kingdom

Correspondence: Simon Pfreundschuh (simon.pfreundschuh@chalmers.se)

Abstract. Remote sensing observations at sub-millimeter wavelengths provide higher sensitivity to small hydrometeors and low water content than observations at millimeter wavelengths, which are traditionally used to observe clouds and precipitation. Hence they are employed increasingly in field campaigns to study cloud microphysics and will be integrated into the global meteorological observing system to measure the global distribution of ice in the atmosphere. A milestone in this development is the launch of the Ice Cloud Imager (ICI) radiometer on board the second generation of European operational meteorological satellites (Metop-SG), which will make sub-millimeter observations of ice clouds available operationally. Observations at these novel wavelengths provide valuable information not only on their own but also in combination with complementary observations at other wavelengths. This study investigates the potential benefits of combining passive sub-millimeter radiometer observations with a hypothetical W-band cloud radar for the retrieval of frozen hydrometeors. Using a simplified cloud-model, the information content of the combined observations is investigated and the capacity of the observations to constrain the microphysical properties of ice hydrometeors is established. A synergistic retrieval algorithm for airborne observations is proposed and applied to simulated observations from a cloud-resolving model. Results from the synergistic retrieval are compared to equivalent radar- and passive-only implementations in order to assess the benefits of the synergistic sensor configurations. The impact of the assumed ice particle shape on the retrieval results is assessed for all retrieval implementations. Although they show greater sensitivity to the assumed particle shape, the synergistic observations can better constrain the microphysics of the cloud, which decreases uncertainties in retrieved ice water content and improves the retrieval of particle number concentrations. Our results also indicate improved sensitivity to liquid cloud water content for the synergistic configuration compared to a passive-only setup. The results of this study demonstrate the potential of the synergistic sensor configuration to improve retrievals of frozen hydrometeors. The developed synergistic retrieval algorithm can be applied with only minor modifications to suitable airborne observations from sub-millimeter radiometers such as the International Sub-Millimetre Airborne Radiometer.

1 Introduction

Ice hydrometeors play an important role for both weather and climate. They influence the Earth's energy budget through their interaction with incoming and outgoing radiation, constitute a part of the global hydrological cycle and are coupled to the

dynamics of the atmosphere in multiple ways (Bony et al., 2015). Because of this, observations of ice clouds are required for understanding the role of clouds in a changing climate (Boucher et al., 2013), to provide information on the dynamical state of the atmosphere in numerical weather prediction (NWP) models (Geer et al., 2017) and to validate climate models (Waliser et al., 2009). Despite this importance, today's global observing system cannot provide accurate information on the global distribution of ice in the atmosphere (Eliasson et al., 2011; Duncan and Eriksson, 2018). A major difficulty of measuring atmospheric ice using remote sensing lies in the large variability of sizes, concentrations and shapes in which ice particles occur in the atmosphere. The wide spectrum of ice crystal sizes, which ranges from micro- to millimeter scales, can only be partially resolved by available space-borne sensors.

Current operational observation systems used to study clouds can be divided into two groups by virtue of their observing frequency and their corresponding capabilities and limitations. Microwave sensors employ wavelengths ranging down to about $1\,\mathrm{mm}$. Compared to the sizes of ice particles, the wavelengths are very long and therefore sensitive only to very large ice particles. At the same time, they provide the advantage of penetrating even thick clouds. Optical and infrared sensors use radiation with wavelengths from around $15\,\mu\mathrm{m}$ down to several hundred nano meters. Although these relatively short wavelengths make them sensitive to small ice particles, their signal saturates for thick clouds, which makes them insensitive to the ice mass further down the line of sight. Although radars and lidars allow detection of lower ice water contents than their passive counterparts, they are ultimately limited by the same principles.

The currently most accurate information on the global distribution of ice water content (IWC) is provided by the CloudSat radar. A main strength of these observations is their vertical resolution, in the order of 500 m. However, the radar lacks scanning capability and the swath width is just 1.5 km wide, to be contrasted with the swath width of passive imagers which is on the order of 1000 km. A potentially less obvious limitation is that CloudSat performs a single-frequency measurement. Since this limits the information per range bin to one degree of freedom, a priori information is required as additional constraint on microphysical properties such as particle size, concentration and shape.

A way to overcome the limitations of single-frequency radars is to combine them with observations from passive sensors, which typically provide measurements at multiple frequencies and a significantly wider swath. Two types of synergies can be distinguished for such an observation scenario: A local synergy, which consists of using the co-located radar and radiometer observations to obtain more accurate hydrometeor retrievals, and the non-local synergy, which uses the vertically resolved radar observations to support passive-only retrievals across the wide swath of the passive sensor. Prominent examples of satellite missions that exploit both of these synergies are the the Tropical Rainfall Measuring Mission (TRMM, Kummerow et al. (1998); Grecu et al. (2004); Munchak and Kummerow (2011)) and the Global Precipitation Measurement (GPM, Hou et al. (2014); Grecu et al. (2016); Kummerow et al. (2015)) mission. Since the principal target of these missions are retrievals of liquid hydrometeors, they make use of sensors at comparably low microwave frequencies and hence provide only limited sensitivity to frozen hydrometeors.

With the upcoming launch of the Ice Cloud Imager (ICI) a new passive microwave sensor will become operational, which is dedicated to observing ice hydrometeors from space. ICI will extend the range of currently available microwave frequencies with channels at 243, 325, 448 and 664 GHz (Eriksson et al., 2020). This will narrow the size-sensitivity gap between the

infrared and traditional microwave sensors by extending the smallest currently available microwave wavelength from 1.6 mm at 183 GHz down to the sub-millimeter domain (0.45 mm at 664 GHz) and significantly improve the size-sensitivity of space-borne microwave observations of clouds. Together with ICI, the newly developed Microwave Imager (MWI) will be flown on the satellites of the Metop-SG program. MWI will complement ICI's observations with measurements at traditional millimeter wavelengths as well as a spectral band around the 118 GHz oxygen line. The observations of MWI, which cover the frequency range from 19 GHz up to 183 GHz, will provide additional sensitivity to liquid and frozen precipitation as well as water vapor.

With ICI sub-millimeter radiometry of clouds will reach operational status. This has of course sparked interest in its potential for studying ice in the atmosphere. The information content and retrieval performance of radiometer observations alone has been studied in detail for column-integrated ice water content (Jiménez et al., 2007; Wang et al., 2017; Brath et al., 2018; Eriksson et al., 2020) as well as for the vertical distribution of ice in the atmosphere (Birman et al., 2017; Grützun et al., 2018; Aires et al., 2019). Although not directly related to ICI, the combination of millimeter and sub-millimeter radiometer observations with active observations from a cloud radar has been investigated by Evans et al. (2005) and Jiang et al. (2019).

In this study, we are interested in the local synergies of co-located MWI/ICI-type radiometer observations combined with observations from a W-band radar. In particular, we aim to answer the question what additional information can be gained from combined observations compared to observations from the radar or MWI and ICI alone. For this, a combined, variational retrieval is developed and applied to simulated observations of scenes from a cloud-resolving model (CRM). An airborne viewing geometry is assumed for the simulations with all sensors pointing at nadir and close-to overlapping antenna beams. Our work extends the previous work by Evans et al. (2005) and Jiang et al. (2019) by comparing the performance of the combined retrieval to that of equivalent radar- and passive-only retrievals, which allows us to quantify the value added by the synergistic observations. In addition to that, the impact of the assumed scattering properties of ice hydrometeors on the retrieval is investigated.

This study consists of two principal parts: In the first part, simulated observations from a simplified cloud model are used to perform a preliminary study of the complementary information content of radar and passive radiometer observations. In the second part, the developed synergistic retrieval algorithm is applied to simulated observations from a CRM to investigate the performance benefits of the combined observations compared to radar- and passive-only configurations. Following this introduction, Section 2 introduces the test data, sensor configuration and the developed retrieval algorithm on which the study is based. This is followed by the experimental results on the information content of the combined observations and the simulated retrieval results in Section 3. The article closes with a discussion of the results in Section 4 and conclusions in Section 5.

2 Methods and data

2.1 Reference cloud scenes

The cloud scenes which are used for the testing of the retrieval were produced by Environment and Climate Change Canada using a high-resolution NWP configuration of the Global Environmental Multiscale (GEM) Model (Côté et al. (1998)). Two test scenes with a horizontal resolution of 1 km and an extent of 800 km were selected. The vertical resolution of the model

scenes varies between 250 and 500 m below an altitude of 18 km and decreases steadily above that. The scenes, displayed in Fig. 1, were chosen with the aim of covering a large range of cloud structures and compositions so as to ensure a realistic assessment of the retrieval. The first test scene, shown in panel (a), is located in the tropical Pacific and contains a mesoscale convective system in the northern half of the scene and its anvil which extends into the southern half. The second scene, shown in panel (b), is located in the North Atlantic and contains an ice cloud in the southern part and a low-level, mixed-phase cloud in the northern part.
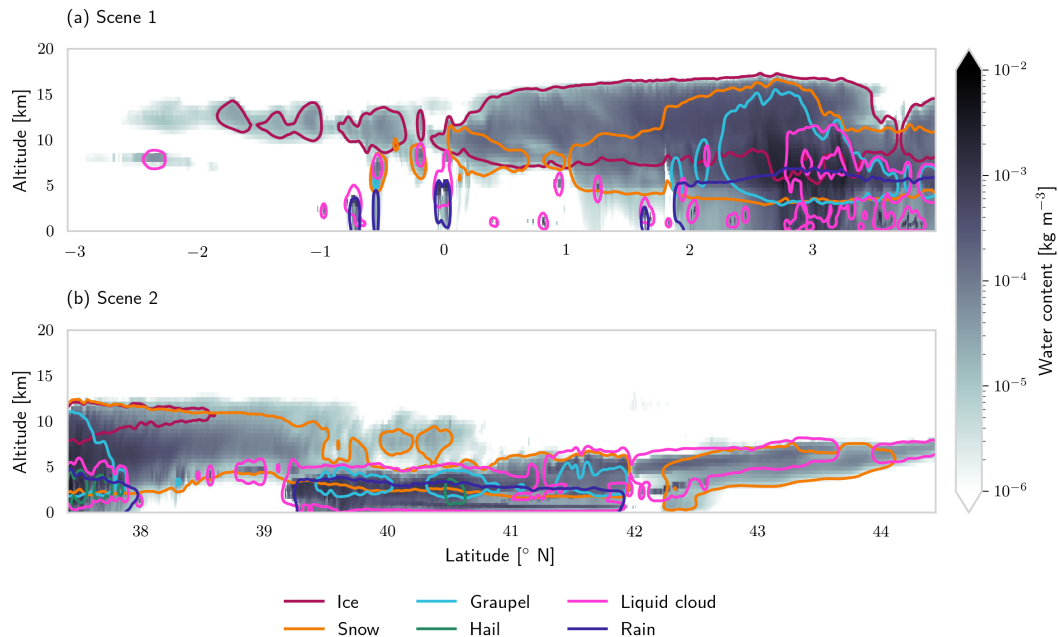

Figure 1. The distribution of total water content including all hydrometeor classes in the two cloud scenes used to test the retrieval. Colored lines show the 10^{-5} kg m^{-3} contour of the water content of each hydrometeor class.

The GEM model uses a two-moment scheme with six types of hydrometeors to represent clouds and precipitation (Milbrandt and Yau, 2005): Two classes of liquid hydrometeors (rain and liquid cloud) and four of frozen hydrometeors (cloud ice, snow, hail and graupel). The particle size distribution (PSD) of each hydrometeor class is described by a three-parameter gamma distribution. The prognostic parameters of the model are the slope and intercept parameters of the PSD, which are derived from the predicted mixing ratios and number concentrations. The third parameter, which defines the shape of the PSD, is set to a fixed, species-specific value. For each hydrometeor species a specific mass-size relationship is assumed.

Examples of particle size distributions of frozen hydrometeors are displayed in Fig. 2. The assumed particle size distributions across different ice species vary mostly in their scaling with respect to size and concentration, whereas the normalized shape shows less variability. An important characteristic of the model can be identified here, which will help to better understand

Table 1. Particle shapes used to represent the hydrometeor species of the GEM model scenes. The mass size relationship is given in terms of the parameters of a fitted power law of the form $m = \alpha \cdot D_{max}^{\beta}$ with D_{max} the maximum diameter and m in kg m^{-3}.

| GEM hydrometeor class | Associated particle shape | Size range | | Mass size relationship | |
	Name (ID)	$D_{eq,\,min}$ [µm]	$D_{eq,\,max}$ [µm]	α	β
Liquid cloud	LiquidSphere (25)	1	$5 \cdot 10^4$	480	3
Rain	LiquidSphere (25)	1	$5 \cdot 10^4$	480	3
Ice cloud	GEM Cloud Ice (31)	10	$3 \cdot 10^3$	440	3
Snow	GEM Snow (32)	94	$5 \cdot 10^3$	24	2.86
Graupel	GEM Graupel (33)	94	$5 \cdot 10^3$	170	2.96
Hail	GEM Hail (34)	94	$5 \cdot 10^3$	540	3.02

the retrieval results presented later: Cloud ice in the model is characterized by high particle number concentrations and small particle sizes, whereas snow has lower number concentrations and larger particles.
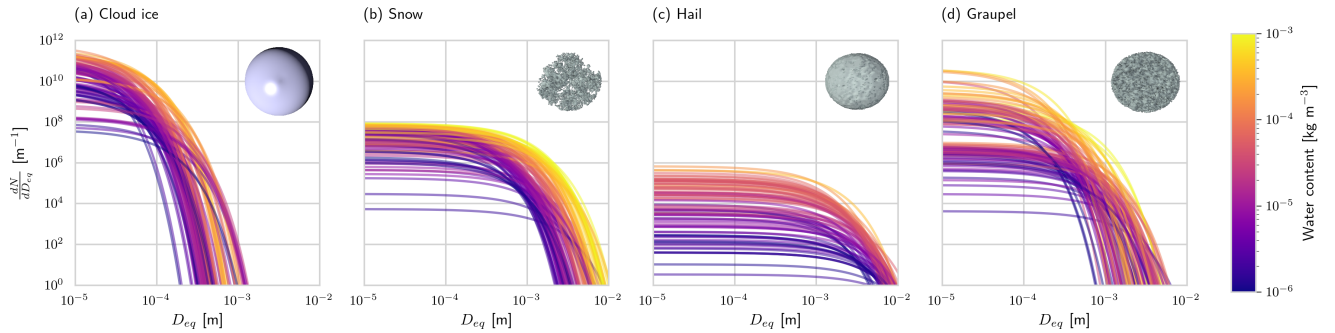

Figure 2. Realizations of particle size distributions from the test scenes used in this study. The particle number concentration is plotted with respect to the volume-equivalent diameter D_{eq}. Shown are the PSDs corresponding to 100 randomly chosen grid points with a water content higher than 10^{-6} kg m^{-3}. Line color encodes the corresponding water content. Inlets display visualizations of the particle shape assumed for each hydrometeor species.

In order to simulate observations from the GEM model scenes, the hydrometeor classes of the GEM microphysics scheme must be associated with particle shapes to define their radiometric properties. The ARTS single-scattering database, described in more detail below, contains particle models which were designed to be consistent with the mass-size relationships assumed in the GEM model. The particle shapes used to represent the GEM model's different hydrometeor types are listed together with their properties in Tab. 1.

2.2 Simulated cloud observations

An airborne sensor configuration is simulated to test the retrieval. The beams of all three sensors are assumed to point at nadir and to be perfectly coincident pencil beams. Multiple scattering effects in the radar observations as well as the effects of particle

orientation are neglected. Although these assumptions may be justified for an airborne configuration, this will not be the case for space-borne observations from ICI and MWI. Moreover, the incidence angles of the beams of ICI and MWI will be around $53°$ at the Earth's surface. This further complicates the radiative transfer modeling since it requires treating a more complex co-location geometry of the nadir-pointing radar and the passive instruments. At off-nadir viewing angles, polarization also needs to be taken into account, the effects of which can be several Kelvin at the typical viewing angles of microwave imagers (Xie et al., 2015).

2.2.1 Sensor configuration

The sensor configuration assumed for the simulated observations includes the 11 highest-frequency channels of the MWI radiometer and all ICI channels. For the radar, a nadir-pointing W-band cloud radar with similar characteristics as the CloudSat Cloud Profiling Radar (CPR, Stephens et al. (2002); Tanelli et al. (2008)) is assumed.

Observations from the ICI radiometer are simulated by performing a single, non-polarized radiative transfer simulation located at the centers of the pass bands of each double-sideband channel and averaging the resulting brightness temperatures. For channels with multiple polarizations, only a single simulation is performed. To compensate for this, the noise of the corresponding channel is reduced by a factor of $\sqrt{2}$. The simulated ICI channels and assumed noise levels are presented in Tab. 2.

Observations from the MWI radiometer are simulated in a similar manner to those of ICI except that for MWI only channels with frequencies larger than or equal to 89 GHz are used. The reason for this is that the footprints of the channels with frequencies lower than 89 GHz will have full-width at half maximum of $50\,\mathrm{km}$ compared to only $10\,\mathrm{km}$ for the MWI's higher-frequency channels and $16\,\mathrm{km}$ for ICI's channels. For a spaceborne configuration, these channels were deemed unlikely to be beneficial for a synergistic retrieval due to the very small overlap of the footprints of these channels with that of the radar. The included MWI channels are listed in Tab. 2.

The frequency of the the cloud radar is chosen to be 94 GHz similar to the CloudSat CPR. The vertical resolution of the nadir-pointing radar observations is assumed to be $500\,\mathrm{m}$ ranging from 0.5 to $20\,\mathrm{km}$ in altitude. The minimum sensitivity is set to be $-30\,\mathrm{dBZ}$ and the noise at each range gate is modeled to be independent with standard deviation $0.5\,\mathrm{dBZ}$.

2.2.2 Radiative transfer simulations

All simulations presented in this study were performed using Version 2.3.1279 of the Atmospheric Radiative Transfer Simulator (ARTS, Buehler et al. (2018)). Radar reflectivities are computed using ARTS' built-in single-scattering radar solver, which provides analytic Jacobians. For the simulation of passive radiances, a hybrid solver is used which combines the DISORT (Stamnes et al., 2000) scattering solver with the ARTS standard scheme for pencil beam radiative transfer. The hybrid solver has been added to ARTS specifically for this study and provides approximate, analytical Jacobians, which are required for variational retrievals of hydrometeors. All simulations are performed assuming an ocean surface with emissivities calculated using the Tool to Estimate Sea-Surface Emissivity from Microwaves to sub-Millimeter waves (TESSEM, Prigent et al. (2017)).

Table 2. Channels of the MWI and ICI radiometers used in the retrieval.

	MWI				ICI	
Channel	Freq. [GHz]	Noise [K]		Channel	Freq. [GHz]	Noise [K]
MWI-8	89	1.1		ICI-1	183.31 ± 7.0	0.8
MWI-9	118.75 ± 3.2	1.3		ICI-2	± 3.4	0.8
MWI-10	± 2.1	1.3		ICI-3	± 2.0	0.8
MWI-11	± 1.4	1.3		ICI-4	243 ± 2.5	$\frac{1}{\sqrt{2}} \cdot 0.7$
MWI-12	± 1.2	1.3		ICI-5	325.15 ± 9.5	1.2
MWI-13	165.5 ± 0.75	1.3		ICI-6	± 3.5	1.3
MWI-14	183.31 ± 7.0	1.2		ICI-7	± 1.5	1.5
MWI-15	± 6.1	1.2		ICI-8	448 ± 7.2	1.4
MWI-16	± 4.9	1.2		ICI-9	± 3.0	1.6
MWI-17	± 3.4	1.2		ICI-10	± 1.4	2.0
MWI-18	± 2.0	1.3		ICI-11	664 ± 4.2	$\frac{1}{\sqrt{2}} \cdot 1.6$

Polarization is neglected in all simulations performed in this study. Gaseous absorption is modeled using the absorption models from Rosenkranz (1993) for N_2, O_2 and from Rosenkranz (1998) for H_2O.

Single scattering data for hydrometeors are taken from ARTS single scattering data base (ARTS SSDB, Eriksson et al. (2018)). The database provides scattering data for a wide range of hydrometeor shapes including particles designed specifically to be consistent with assumptions of the GEM microphysics scheme. It also provides a number of predefined habit mixes, referred to as standard habits, designed to cover the full range of particle sizes relevant for microwave observations of ice hydrometeors.

2.3 Retrieval algorithm

A one-dimensional, variational cloud retrieval algorithm is proposed which uses the optimal estimation method (OEM, Rodgers (2000)) to fit an atmospheric state to given observations. The quality of a retrieved state $\hat{\mathbf{x}}$ and corresponding simulated observations $\hat{\mathbf{y}} = \mathbf{F}(\hat{\mathbf{x}})$ is assessed using the following diagnostic quantity:

$$\chi_y^2 = \Delta \mathbf{y}^T \mathbf{S}_e^{-1} \Delta \mathbf{y} \tag{1}$$

Here, $\Delta \mathbf{y} = \mathbf{y} - \hat{\mathbf{y}}$ is the difference between the fitted and true observations and $\mathbf{S}_e$ is the covariance matrix describing the measurement errors. The quantity χ_y^2 corresponds to the sum of squared errors in the fitted observations weighted by the uncertainties in each channel or range bin. It should be noted that the quantity has no meaningful interpretation in terms of χ^2-statistic for the errors in the fitted observations since they will neither be independent (c.f. Chapter 12 in Rodgers (2000)) nor Gaussian due to the presence of forward model error. The value is therefore used here solely as a heuristic to quantify the goodness of the fit to the true observations.
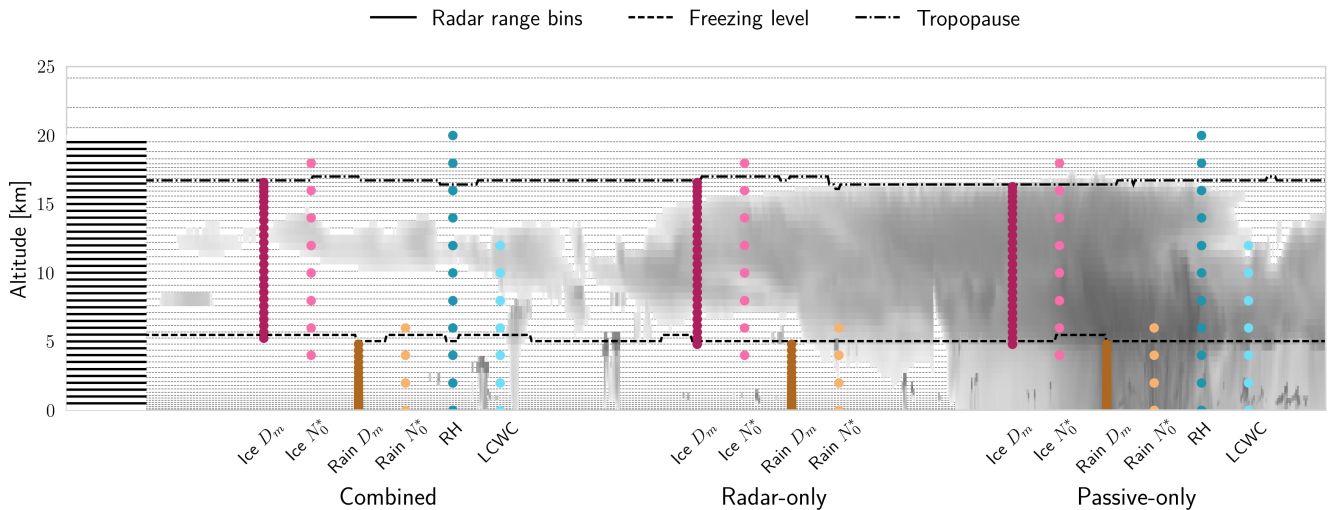
Figure 3. Illustration of retrieval quantities and their respective retrieval grids. Grey, dashed lines in the background display the vertical grid of the GEM model. Black, solid lines on the left side display the range bins of the radar observations. Filled markers represent the retrieval grids of each retrieval quantity for the combined, radar-only and passive-only configurations of the retrieval algorithm.

2.3.1 Measurement space

The input for the synergistic retrieval is the combined observation vector **y** consisting of the concatenated single-instrument observations from the cloud radar and the two radiometers. Measurement errors are assumed to be independent and Gaussian distributed with standard deviations according to the noise characteristics given in Section 2.2.1. For the single-instrument retrievals the measurement vector consists only of observations from either the radar or the radiometers.

2.3.2 State space

The proposed retrieval solves for profiles of two degrees of freedom of the PSDs of frozen hydrometeors and rain along with profiles of relative humidity (RH) and liquid-cloud water content (LCWC). An illustration of the retrieved quantities and their respective retrieval grids for the combined and single-instrument configurations of the retrieval are given in Fig. 3.

The PSDs of frozen hydrometeors and rain are represented using the normalized particle size distribution formalism proposed by Delanoë et al. (2005). The PSD of a hydrometeor species at a given altitude is modeled using a generalized gamma distribution function with four parameters. The mass-weighted mean diameter D_m, which scales the PSD along the size dimension, and the normalized number density N_0^*, which scales the particle concentration, are the two retrieved degrees of freedom of the PSD. The other two parameters describe the shape of the normalized PSD. The same shape parameters as in version 3 of the DARDAR-CLOUD product (Cazenave et al., 2019) are chosen for frozen hydrometeors. For rain, they are chosen to match the shape used in the GEM model for rain drops.

8

The temperature-dependent a priori profile for N_0^* for frozen hydrometeors is determined using the relation from Delanoë et al. (2014)

$$N_0^* = \exp\left(-0.076586 \cdot (T - 273.15) + 17.948\right),$$ (2)

where T is in K. The a priori profile of D_m for frozen hydrometeors is chosen so that the a priori IWC is equal to 10^{-6} kg m^{-3}. For rain, a fixed value for N_0^* of 10^6 m^{-4} is assumed and the a priori profile for D_m is determined similarly as for frozen hydrometeors.

Since the N_0^* parameters vary over several orders of magnitude they are retrieved in $\log_{10}$-space for both frozen hydrometeors and rain. The D_m parameters, in contrast, are retrieved in linear space. Alternative parametrizations using water content and D_m or the water content and N_0^* have been tested but no considerable effect on retrieval performance has been observed. As additional constraints, the retrieval of frozen hydrometeors is restricted to the region between the freezing level, here defined simply as the 273.15 K-isotherm, and the approximate altitude of the tropopause. The altitude of the tropopause is approximated as the first grid point at which the lapse rate is negative and temperature below 220 K. The retrieval of rain hydrometeors is restricted to below the freezing level. The retrieval of the N_0^* parameters is further regularized by retrieving them at reduced vertical resolution of 2 km. This was found necessary to keep the retrieval from getting stuck in spurious local minima. This resembles the approach taken in the GPM combined precipitation retrievals (Grecu et al., 2016), where the PSD parameter scaling the particle concentration is also retrieved at reduced resolution.

Relative humidity is retrieved at a vertical resolution of 2 km. However, the values are not retrieved directly but instead an inverse hyperbolic tangent transformation is applied to the relative humidity profile:

$$x = \operatorname{arctanh}\left(\frac{2\mathrm{RH}}{1.2} - 1.0\right)$$ (3)

The transformation restricts the retrieved relative humidity values to the range between 0 and 120%. The a priori profile for relative humidity is set to

$$\mathrm{RH}(t) = \begin{cases} 0.7 & , 270\,\mathrm{K} < t \\ 0.7 - 0.01 \cdot (270 - t) & , 220 < t \leq 270\,\mathrm{K} \\ 0.2 & , t < 220\mathrm{K} \end{cases}$$ (4)

LCWC is retrieved at a resolution of 2 km but is restricted to the region between the surface and the 230 K isotherm. In contrast to frozen hydrometeors and rain, the PSD of liquid cloud droplets is not explicitly resolved in the retrieval forward model. Instead, liquid cloud droplets are modeled as purely absorbing quantity using the model by Liebe et al. (1993) for suspended liquid cloud droplets. Note that this is the case only for the retrieval. For the simulated observations, liquid cloud droplets are handled as any other hydrometeor species in the GEM model. LCWC is retrieved in $\log_{10}$-space and the a priori profile is set to a fixed value of 10^{-6} kg m^{-3} in the permitted region of the atmosphere.

The a priori distributions of the 6 retrieval quantities (N_0^* and D_m for frozen and liquid hydrometeors, RH, CLWC) are assumed to be independent so that the overall a priori covariance matrix $\mathbf{S}_a$ has block-diagonal structure. Within each block,

vertical correlations between the values of a given retrieval quantity at different altitudes are assumed to be exponentially decaying. The covariance of the values of retrieval quantity q at points i and j of the retrieval grid is computed as

$$(\mathbf{S}_{a,q})_{i,j} = \sigma_{q,i}\sigma_{q,j} \cdot \exp\left(-\frac{d(i,j)}{l_q}\right), \tag{5}$$

where $\sigma_{q,i}$ is the a priori uncertainty assumed for retrieval quantity q at grid point i, $d(i,j)$ the vertical distance between the grid points and l_q the quantity-specific correlation length. The assumed a priori uncertainties and correlation lengths for the retrieval quantities are summarized in Tab. 3.

Table 3. A priori uncertainties and correlation lengths used in the retrieval.

Retrieval target		Combined / Radar-only		Passive-only	
Name	Retrieved quantity	σ_q	l_q [km]	σ_q	l_q [km]
Ice, N_0^*	$\log_{10}(N_{0,\mathrm{Ice}}^*)$	2	2	2	5
Ice, D_m	Ice $D_{m,\mathrm{Ice}}$	300 µm	2	300 µm	5
Rain, N_0^*	$\log_{10}(\mathrm{Rain}\ N_0^*)$	2	2	2	5
Rain, D_m	$D_{m,\mathrm{Rain}}$	300 µm	2	300 µm	5
Relative humidity (RH)	$\mathrm{arctanh}(\frac{2\cdot\mathrm{RH}}{1.2} - 1.0)$	0.5*	2*	0.5	2
Cloud liquid water content (CLWC)	$\log_{10}(\mathrm{CLWC})$	1*	2*	1	2

*: Not retrieved in radar-only retrieval

The radar-only version of the retrieval is similar to the combined version except that RH and LCWC are not retrieved. Instead, perfect knowledge of the true RH profile is assumed while LCWC is neglected. In addition to a two-moment radar-only retrieval, also a one-moment version (M1), in which only the D_m parameter is retrieved has been tested. For completeness, retrieval results for IWC will be reported also for the M1 version. However, to allow for better comparison with the combined and passive-only retrieval, for the remaining results only the two-moment version is considered. For the passive-only retrieval, the retrieval quantities and grids are the same as for the combined retrieval. However, higher correlations lengths are assumed, which are shown in Tab. 3

2.3.3 Representation of ice particle shape

A major difficulty for cloud retrievals is that the observations may not provide sufficient information to distinguish different hydrometeor species. Due to this ambiguity, frozen hydrometeors in the proposed retrieval algorithm are represented using only a single hydrometeor species. It is therefore necessary to find a suitable representation for frozen hydrometeors, which can capture the variability of the four frozen hydrometeor species in the GEM model and ideally also that of real ice hydrometeors.

The differences between hydrometeor species in the test scenes are due to their different concentrations, sizes and shapes (c.f. Fig. 2). Since two parameters of the PSD of frozen hydrometeor species are retrieved, the retrieval is able to represent the characteristic number concentrations and particle sizes of different hydrometeor species. Variations in particle shape which correlate with particle size can be represented using a habit mix combining crystal shapes at small sizes with aggregates or

235 rimed particles at larger sizes. This provides the retrieval with some flexibility to represent the different shapes present in the test scenes.

Even with this configuration the simplified retrieval forward model will not be able to represent every possible configuration of mixes of the four ice hydrometeor species in the GEM model. It thus remains unclear which particle shape should be used to best represent this mixture. We therefore choose a set consisting of multiple particle shapes and habit mixes for which we

240 investigate the impact of the particle choice on the retrieval results. The selected particles are listed in Tab. 4. Three of them, GEM Cloud Ice, GEM Snow, and GEM Graupel, correspond to the shapes present in the GEM model scenes. The GEM Snow and Graupel habits were mixed with crystal shapes to ensure that they cover sizes down to around $10\,\mu$m. In addition to this, two of the habit mixes distributed with the ARTS SSDB, the Large Plate Aggregate and Large Column Aggregate standard habits, are included in the selection to increase the range of scattering properties it covers. Fig. 4 provides an overview of the

245 bulk mass backscattering efficiencies and mass attenuation coefficients of the selected particles computed for three different values of the N_0^* parameter of the PSD. Mass backscattering efficiency and attenuation coefficient are defined as the ratio of the corresponding cross-section σ and the bulk water content:

$$Q = \frac{\sigma}{\mathrm{WC}} \tag{6}$$

For high values of N_0^*, which are typical for cloud ice, the radiometric properties of particle shapes differ only for large masses

250 at the two highest frequencies considered. For low N_0^* values, which are more typical for snow, the particles' properties differ considerably at all masses and frequencies. At the two lowest frequencies, the Large Column Aggregate, Large Plate Aggregate and GEM Snow are the least efficient scatterers or absorbers of radiation whereas GEM Graupel, Gem Hail and GEM Cloud Ice are more efficient. This behavior is also observed at the two higher frequencies, except for the lowest N_0^* value for which a reversal of the ordering occurs as the bulk mass increases. The mass backscattering efficiency at $94\,$GHz shows the greatest

255 relative variability across different bulk water contents and N_0^* values, spanning six orders of magnitudes, while for the mass attenuation coefficients at the other frequencies the variability spans at most three orders of magnitude.

3 Results

The first part of this section presents results from a numerical experiment which investigates the complementary information content of the active and passive microwave observations. Results of the combined and the single-instrument retrievals applied

260 to the reference cloud scenes are presented in the second part.

3.1 Complementary information content

A fundamental question regarding the benefit of combining two remote sensing observations in a retrieval is to what extent the observations contain non-redundant information. The degree of non-redundancy in the combined observations is what we refer to here as complementary information content. We are thus interested in the information that cannot be provided by either of
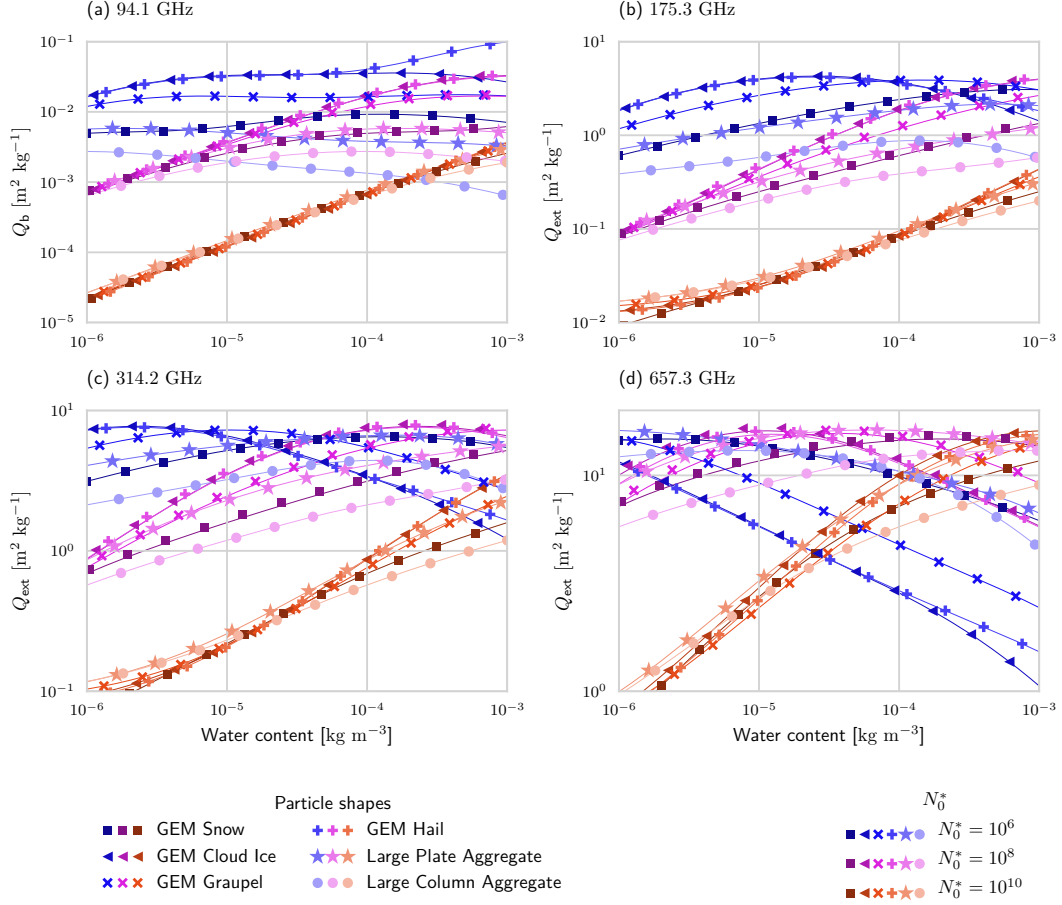
11

Figure 4. Bulk mass backscattering efficiency Q_b at 94.1 GHz (a) and mass attenuation coefficients Q_e at frequencies 175.3 GHz (b), 314.2 GHz (c) and 657.3 GHz (d) for the particle models used in the simulated observations and the retrieval. Different colors show the bulk properties for different values of the N_0^* parameter of the PSD.

Table 4. Particle models used to represent ice hydrometeors used in the retrieval. The mass size relationship is given in terms of the parameters of a fitted power law of the form $m = \alpha \cdot D_{\max}^{\beta}$ with $D_{\max}$ the maximum diameter and m in kg m^{-3}.

Name	Shapes used	Size range		Mass size relationship	
	Name (ID)	$D_{\mathrm{eq,\,min}}$ [μm]	$D_{\mathrm{eq,\,max}}$ [μm]	α	β
CloudIce	GEM CloudIce (11)	10	3000	440	3
GEM Snow	8-Column Aggregate (8)	10	127	65	3
	GEM Snow (32)	107	5000	24	2.86
GEM Graupel	8-Column Aggregate (8)	10	179	65	3
	GEM Graupel (33)	107	5000	170	2.96
Large Plate Aggregate	Thick Plate (15)	16	200	110	3
	Large Plate Aggregate (33)	160	3021	0.21	2.26
Large Column Aggregate	Block Column (12)	10	200	110	3
	Large Column Aggregate (22)	160	3021	0.25	2.43

265   the instruments alone. The higher resolution achieved by adding radar observations to passive ones is therefore not considered as complementary information since the radar alone can provide the increased resolution.

In order to explore the complementary information content in the radar and radiometer observations, an idealized, homogeneous cloud layer with a thickness of 5 km centered at an altitude of 10 km in a tropical atmosphere is considered. The cloud is assumed to consist of a single species of frozen hydrometeors represented using the PSD parametrization which is also used

270   in the retrieval and described in Sec. 2.3.2. As particle model, the 8-Column Aggregate (ID 8) from the ARTS SSDB is used.

The question that is addressed here is whether the combination of active and passive observations is able to constrain both the size and concentration of the ice particles in the cloud. To investigate this, the N_0^* and D_m parameters of the homogeneous cloud layer are varied and observations of the cloud are simulated. The cloud signal in the radiometer observations is the difference between the cloudy- and clear-sky brightness temperatures (ΔT_B). The signal in the active observations is here

275   defined as the maximum of the measured profile of radar reflectivity dBZ$_{\max}$. Figure 5 displays the contours of ΔT_B and dBZ$_{\max}$ with respect to D_m and the cloud's water content, which is proportional to N_0^*:

$$\mathrm{WC} = \frac{\pi \rho}{4^4} N_0^* D_m^4, \tag{7}$$

with ρ the density of ice.

Along the dBZ$_{\max}$-contours the cloud composition changes but the observed signal stays the same. This shows the ambiguity

280   of the radar observations with respect to the cloud composition. A necessary condition for a passive observation at a given frequency to be able to resolve this ambiguity is that the contours of the active and passive signals cross each other. The panels in Fig. 5 thus provide an indication to what extent the information in the radar measurement and the corresponding passive radiometer channel provide complementary information on the two degrees of freedom of the PSD. The results show that the MWI channels provide complementary information only for very dense clouds consisting of large particles. In contrast to
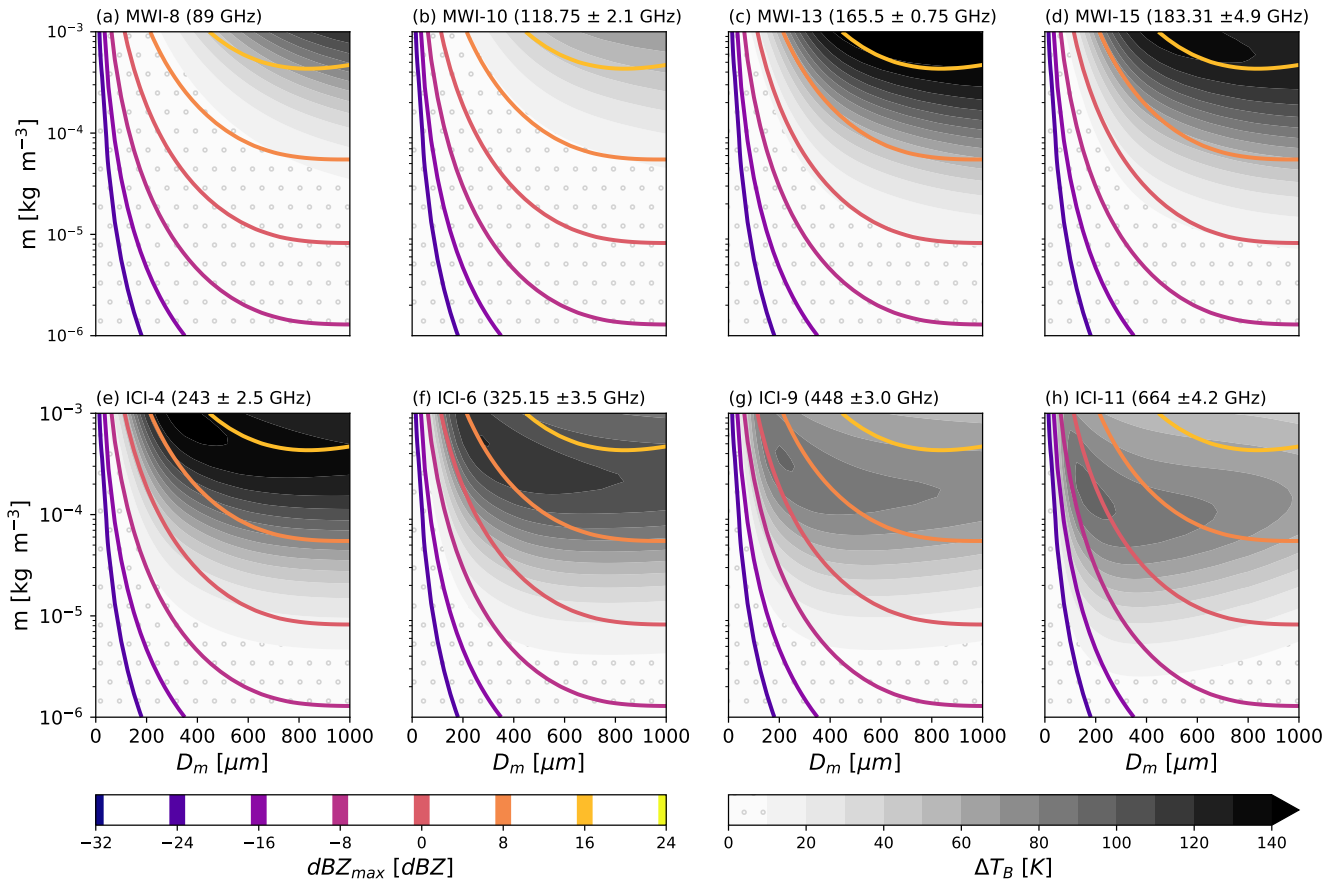
Figure 5. Simulated observations of a homogeneous, 5 km thick cloud layer centered at 10 km with varying water content m and mass-weighted mean diameter D_m. The panels display the maximum radar reflectivity in dBZ (dBZ$_{max}$) overlaid onto the cloud signal (ΔT_B) measured by selected radiometer channels of the MWI (first row) and ICI radiometers (second row).

that, the ICI observations exhibit crossing contours already at lower water content and D_m values, indicating complementary information for less dense clouds and smaller particles.

3.2 Retrieval results

To assess the performance of the combined cloud retrieval, the developed algorithm has been applied to the two designated cloud scenes. The same retrievals have been performed with a radar-only and a passive-only version of the algorithm to serve as baselines for the evaluation of the combined retrieval. Each retrieval was performed multiple times using the different ice particle models listed in Tab. 4. Since the results for both test scenes are qualitatively similar, results from the second scene are provided in App. A. Complete results for all retrieval quantities, both scenes and all tested particle shapes are provided as digital supplement to this article.
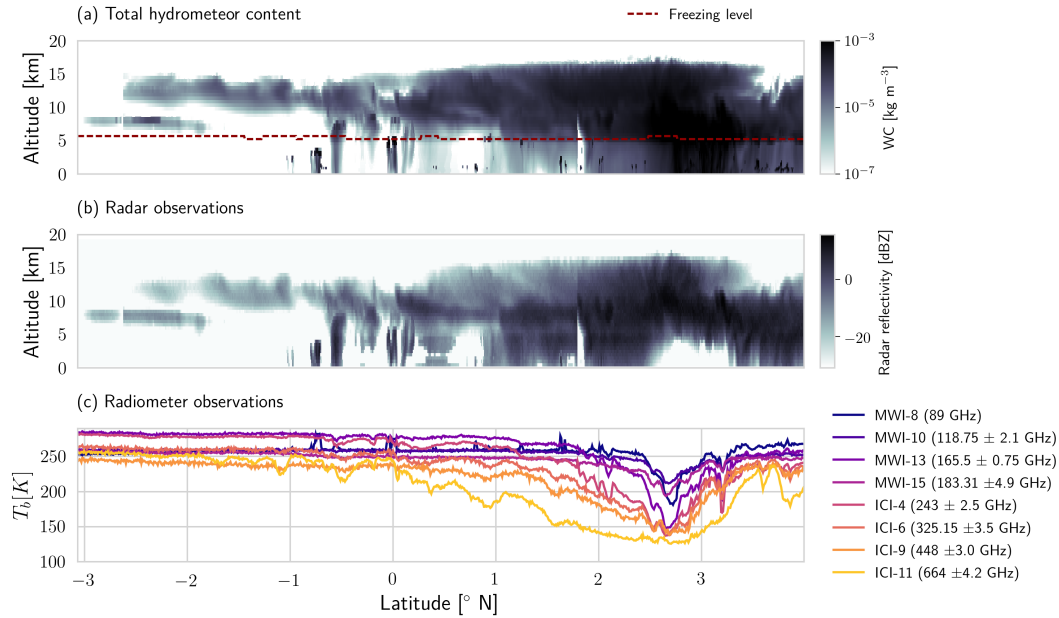
Figure 6. Total water content (WC) and simulated observations for the first test scene. Panel (a) displays the total water content in the scene, i.e. the sum of the water content of all hydrometeor species of the GEM model. Panel (b) shows the simulated radar reflectivities. Panel (c) displays the simulated brightness temperatures for a selection of channels of the MWI and ICI radiometers.

The simulated observations which were generated to test the retrievals are shown for the first test scene in Fig. 6. Independent Gaussian noise with standard deviations according to sensor specifications has been added to the simulated observations to account for sensor noise. It is important to note that the simulated observations used to test the retrieval assume different microphysics than what is assumed in the retrieval. The synthetic observations are computed using the six hydrometeor classes from the GEM model, while the retrieval forward model assumes only two classes of hydrometeors.

3.2.1 Water content

Retrieved IWC obtained using the Large Plate Aggregate particle model for the first test scene is displayed together with the reference IWC field in Fig. 7. The reference IWC is defined here as the sum of the masses of the four frozen hydrometeor species in the GEM model scenes.

The normalized χ_y^2 values of the three retrieval configurations, displayed in Panel (a), give an indication of how well the retrievals are able to fit the observations. For the radar-only retrieval, the values are much smaller than 1 for most parts of the scene, while for the passive-only and combined retrieval they are around the expected value of 1. This indicates that the radar-only retrieval overfits the observations, while the passive-only and combined retrievals achieve the expected fit. The exception is the region around $3°\ N$, where the cloud is particularly thick and consists of a mix of different hydrometeor types. Here, especially the passive-only retrieval has problems fitting the observations.

15

In terms of IWP, all methods provide fairly good estimates of the reference values with the combined retrieval consistently yielding the smallest deviations. Larger differences between the methods are observed when comparing the retrieval results in terms of IWC. While the vertical structure of the cloud is captured only very roughly by the passive retrieval, it is better resolved by the radar-only and the combined retrieval. On closer inspection, however, it becomes evident that the radar-only retrieval deviates systematically from the reference IWC in specific regions of the cloud, such as for example the upper part of the cloud between $0°N$ and $2°N$. These deviations are corrected in the results from the combined retrieval, however certain retrieval artifacts remain visible.

For a more quantitative assessment of the retrieval performance, retrieved water content is plotted against the reference water content in Fig. 8. In terms of precision, the passive-only retrieval performs worst while both the radar-only and combined retrieval yield much smaller spread in the retrieved values. This is not surprising considering that the passive observations do not contain sufficient information on the vertical distribution of IWC to yield accurate results at the resolution of the model scenes. In terms of overall accuracy, i.e. systematic deviations from the diagonal, no clear differences between the three configurations are visible. However, the color-coding with respect to hydrometeor species reveals that the radar-only retrieval is biased for specific hydrometeor classes. In the combined and even the passive-only results, this effect is weaker and the clusters are generally moved towards the diagonal. For graupel, all retrievals perform badly but this is likely due to it being present only in the core of the convective system where the signals from all sensors can be expected to be saturated.

Comparing the results for different particle models, a clear dependency is evident in the passive-only and the combined results while the radar-only retrieval is affected the least. For the combined and passive-only retrieval, the effect is consistent across the methods, with the GEM Cloud Ice and Large Column Aggregate yielding the largest deviations and the Large Plate Aggregate yielding the most accurate results.

To summarize retrieval performance for all tested retrieval methods and particle shapes, the distributions of the logarithmic error

$$E_{\log_{10}} = \log_{10}\left(\frac{x_{\text{retrieved}}}{x_{\text{reference}}}\right) \tag{8}$$

for the retrieved IWC and IWP are displayed in Fig. 9. In addition to the two-moment version of the radar-only retrieval, this figure also displays results of the single-moment version of the retrieval, which was actually found to yield better IWC retrievals for the second test scene.

The error for IWC has been computed considering only grid points where either reference or retrieved IWC is larger than $10^{-6}\,\text{kg}\,\text{m}^{-3}$. Similar to the results presented above, the combined retrieval yields the smallest retrieval errors for suitable choices of the particle model. Although the two-moment radar-only retrieval performs similar to the combined retrieval in terms of precision, it yields significant systematic errors for the second scene. The reason for this can be understood considering the cloud composition displayed in Fig. 1. Since the clouds in the second test scene consist mostly of snow, the bias of the radar-only retrieval with respect to this specific hydrometeor species (c.f. Fig. 8 and also Fig. A2) leads to the large observed systematic errors for the second scene. The single-moment radar-only retrieval does not produce the same large systematic
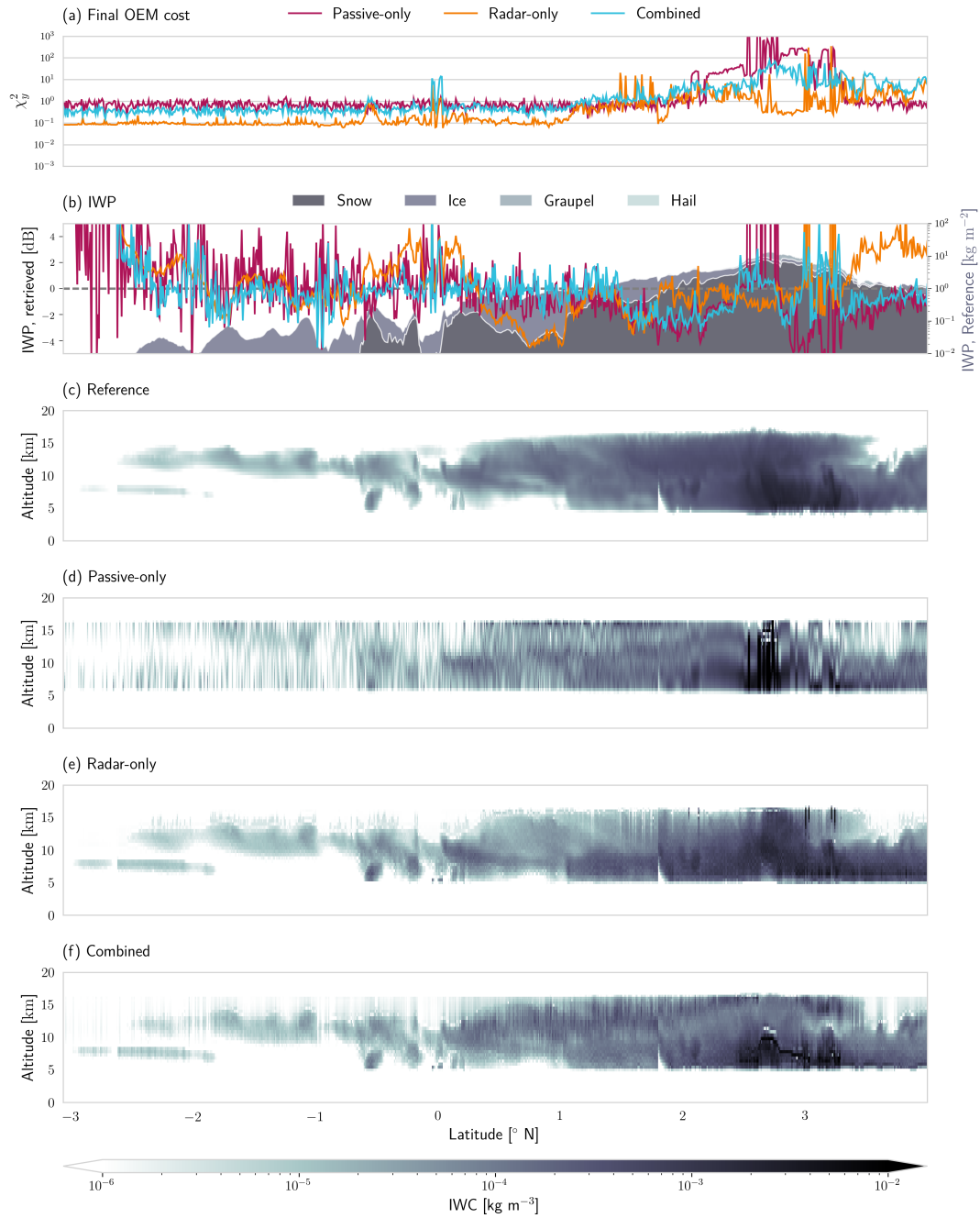
Figure 7. Results of the ice hydrometeor retrieval for the first test scene using the Large Plage Aggregate particle model. Panel (a) displays the value of the χ^2_y diagnostic normalized by the dimension of the measurement space of the corresponding retrieval. Panel (b) displays retrieved IWP in dB relative to the reference IWP. Reference IWP and the contributions from different hydrometeor classes are displayed by the filled areas in the background. Panel (c) shows the reference IWC from the model scene. Panel (d), (e) and (f) display the retrieval results for the passive-only, radar-only and combined retrieval, respectively.
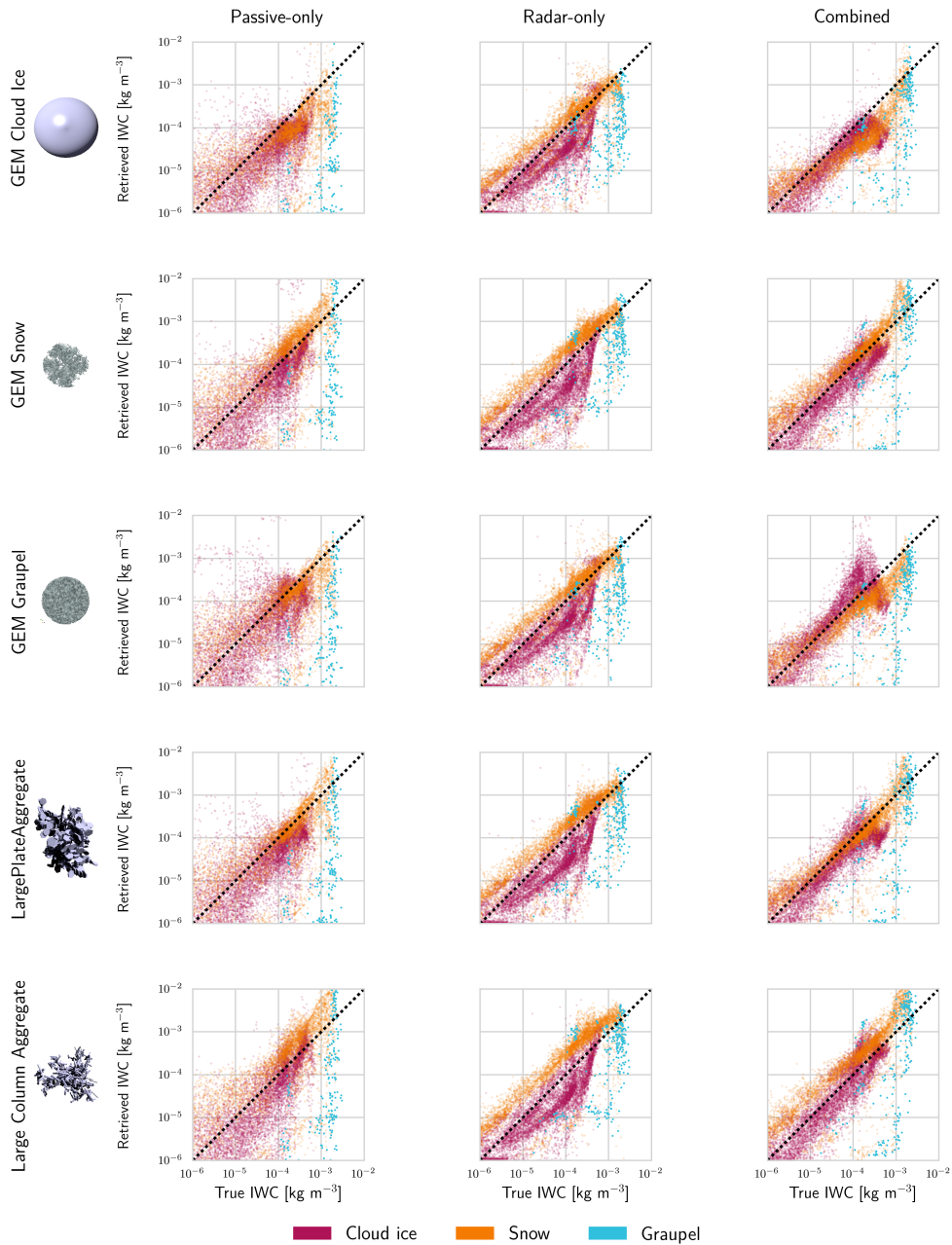
Figure 8. Retrieved IWC plotted against reference IWC for the tested retrieval configurations. Each row shows the retrieval results for the particle shape shown in the first panel. The following panels show the retrieval results for the passive-only (first column), the radar-only (second column) and the combined retrieval (third column). Markers are colored according to the prevailing hydrometeor type at the corresponding grid point in the test scene. Due to their sparsity, markers corresponding to graupel are drawn at twice the size of the other markers.

errors for the second scene, but instead produces systematic errors for the first scene. The passive-only retrieval yields the largest errors in terms of retrieved IWC due its low vertical resolution.

In terms of IWP, however, the errors of the passive-only retrieval are decreased making the retrieval comparable to the other
345 methods. For the radar-only and combined retrievals, the precision is generally increased but the systematic deviations observed for IWC persist. This leads, particularly for the second test scene, to significant systematic errors in the IWP retrieved by the two-moment radar-only retrieval.

Also in these results, a strong dependence on the applied particle model is observed for the passive-only and combined retrievals. The errors are particularly large for the GEM Cloud Ice and the Large Column Aggregate. Although the impact is
350 stronger for the M1 version, the particle shape has less impact on the retrieval performance of the radar-only retrieval and does not affect the large systematic errors observed for the second test scene.
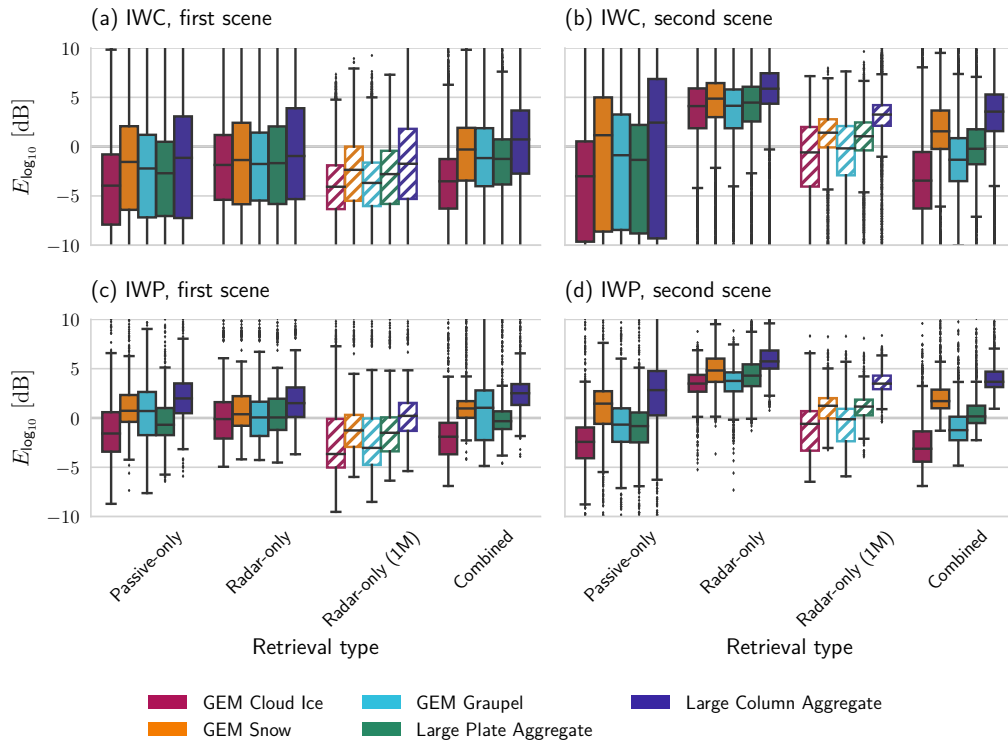
Figure 9. Distributions of the logarithmic retrieval error in IWC and IWP for all tested retrieval methods and particle shapes displayed as box plots. Colored boxes display the interquartile range (IQR) while whiskers show the full range of all points not considered outliers. Points whose distance to the IQR is larger than 1.5 times the width of the IQR are considered outliers and drawn as markers. Two results are shown for the radar-only retrieval, one for the standard version retrieving both PSD moments (solid boxes) and one for the single-moment (1M) version (diagonal hatches).

3.2.2 Particle number concentrations

Particle number concentrations of frozen hydrometeors have been derived from the retrieved N_0^* and D_m parameters by computing the zeroth moment of the corresponding PSD. The resulting particle number concentration fields are displayed together with the reference field in Fig. 10. To simplify the comparison, number concentrations are displayed only where the corresponding reference or retrieved IWC is larger than 10^{-6} kg m^{-3}.

Comparing the passive-only and the radar-only retrieval to the reference fields shows that both methods have little to no skill in predicting number concentrations. Although the passive-only retrieval partly captures the gradient between very high concentrations at the top of the cloud and the low concentrations at the bottom, it is not at all resolved in the radar-only retrieval.

In contrast to this, the combined retrieval manages to reproduce this gradient in most parts of the scene. The strongest deviations of the combined results from the reference field are observed between 2 ° N and 3° N latitude. Here, the results strongly underestimate the true number concentrations. Comparison with the cloud composition displayed in Panel (a) of Fig. 1 shows that this region contains large amounts of both cloud ice and snow. The retrieval uses only a single hydrometeor species to represent ice in the atmosphere and is therefore not able to represent such heterogeneous conditions. Since snow will have a stronger impact on the observations, the retrieval in these regions will likely tend to represent snow rather than ice, which leads to the low retrieved number concentrations.

Fig. 11 displays scatter plots of the reference and retrieved particle number concentrations for all three methods and two particle models from the first test scene. Markers in the plot are color coded according to their homogeneity in the reference scene, here defined as the ratio of the maximum water content of any of the frozen hydrometeor species and the total water content. These results confirm that the passive-only retrieval possesses some sensitivity to the particle number concentrations since the cluster at low concentrations corresponding to snow is placed correctly on the diagonal, which is not the case for the radar-only retrieval. The radar-only retrieval does not exhibit any retrieval skill, hardly reproducing any of the variation of the reference values. Contrary to this, the combined retrieval moves both clusters, the one corresponding to snow and the one at high number concentrations corresponding to cloud ice, towards the diagonal. This indicates that it is capable of distinguishing the microphysical properties of cloud ice and snow. Furthermore, the color coding shows that the strongest deviations between retrieved and reference number concentrations occur for grid points where the cloud composition is heterogeneous.

The general effect of particle shape on the retrieval results is similar to what has been observed for IWC, which is why only results for two particle shapes are shown. For the passive-only and combined retrieval, the GEM Cloud Ice and Large Column Aggregate models yield the worst retrieval results, while the Large Plate Aggregate performs best. For the radar-only retrieval no noticeable differences are observed between different particle models.

3.2.3 Information content

To quantify the information content of the single-instrument and the combined observations, the degrees of freedom for signal (DFS) have been computed following Rodgers (2000) by calculating the trace of the averaging kernel matrix

$$\mathbf{A} = (\mathbf{K}^T \mathbf{S}_e^{-1} \mathbf{K} + \mathbf{S}_a^{-1})^{-1} \mathbf{K}^T \mathbf{S}_e^{-1} \mathbf{K}, \tag{9}$$
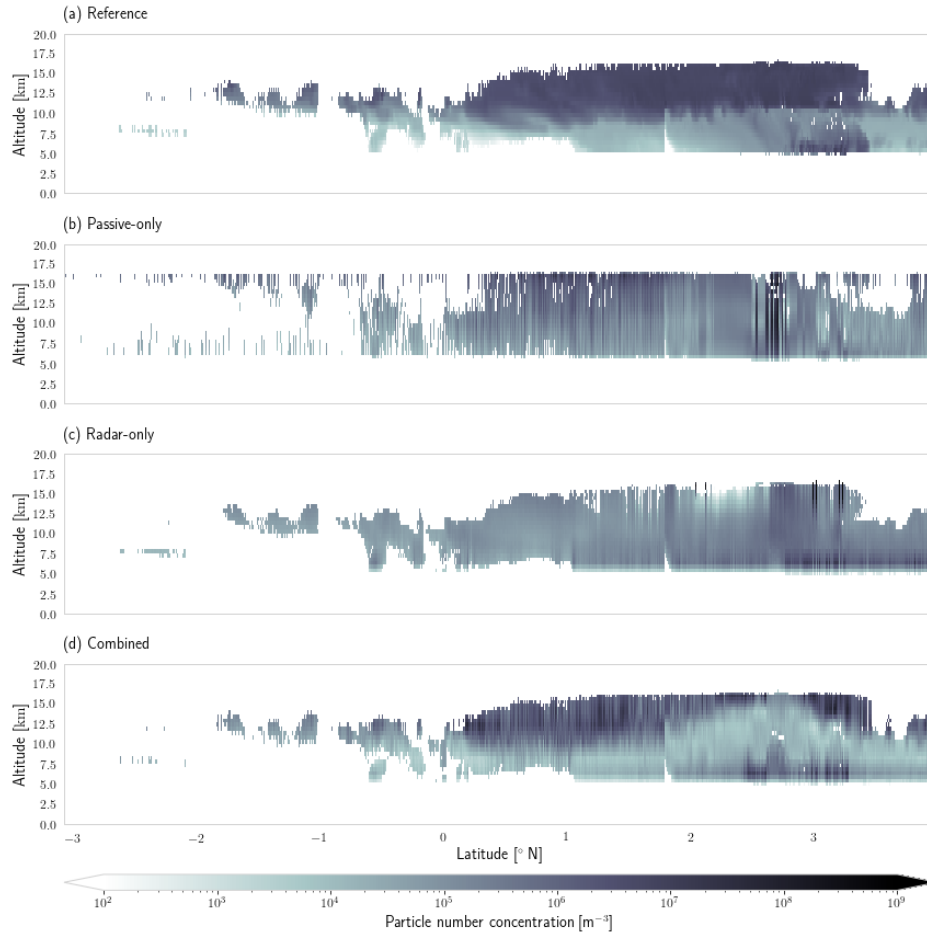
Figure 10. Reference and retrieved particle number concentrations of frozen hydrometeors for the first test scene obtained with the Large-PlateAggregate particle model. Panel (a) displays the reference water content from the model scene. Panel (b), (c) and (d) display the retrieval results for the passive-only, radar-only and combined retrieval. Only values for which the corresponding reference or retrieved IWC was larger than 10^{-6} kg m^{-3} are shown here.
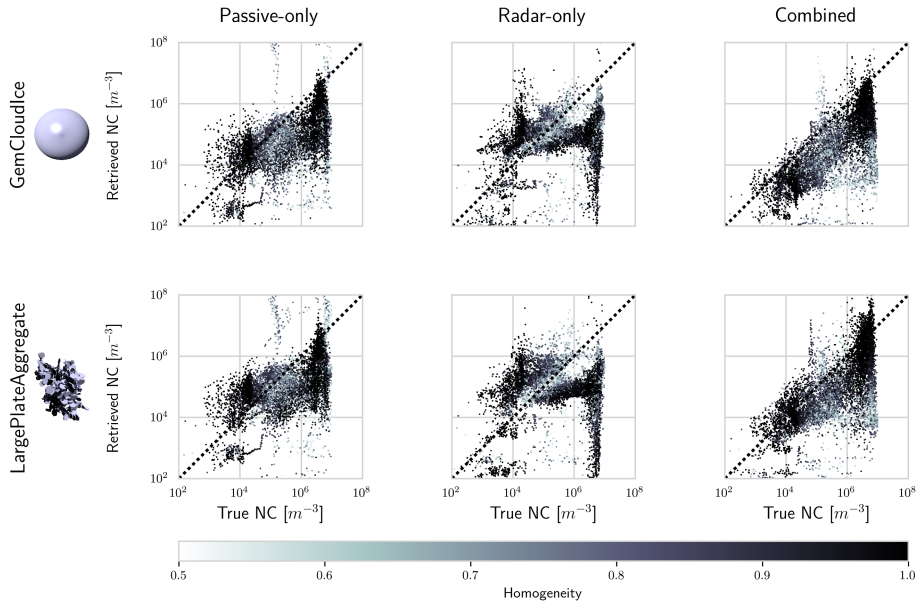
Figure 11. Scatter plots of the retrieved particle number concentrations at grid points with reference IWC larger than 10^{-5} kg m^{-3}. Rows show the results for the different particle models used in the retrieval while columns display results for different retrieval methods. The marker color encodes the homogeneity of the corresponding ice mass, which is computed as the ratio of the maximum water content of any of the frozen hydrometeor species and total IWC.

where $\mathbf{K} = \frac{d\mathbf{F}(\mathbf{x})}{d\mathbf{x}}$ is the Jacobian of the forward model. The information content and its decomposition into contributions from different retrieval quantities are displayed in Fig. 12.

With respect to ice, the passive-only retrieval yields the lowest information content. For the radar-only retrieval the information content is significantly higher, on the order of 20 degrees of freedom, but the major part of it is attributed to the D_m parameter. For the combined retrieval, the total information content on ice hydrometeors is increased compared to the radar-only retrieval in regions where the passive-only retrieval provides information on frozen hydrometeors. In addition to that, a clear shift of information content from D_m to N_0^* can be observed over both scenes.

The information content for rain is much smaller but in relative terms the general behavior is the same as for ice. For RH, no difference is observed for the information content provided by the passive-only and combined retrievals. For LCWC, the information content of the combined observations is increased slightly but remains limited to a few degrees of freedom.

3.2.4 Impact of assumed ice particle shape

The impact of the assumed ice particle shape on the retrieval results raises the question whether it also affects the quality of the fit to the observations. To investigate this, the residuals for the radar observations and three ICI channels are displayed in Fig. 13. Each test scene contains a region where the retrieval does not fit the observations well and where substantial deviations
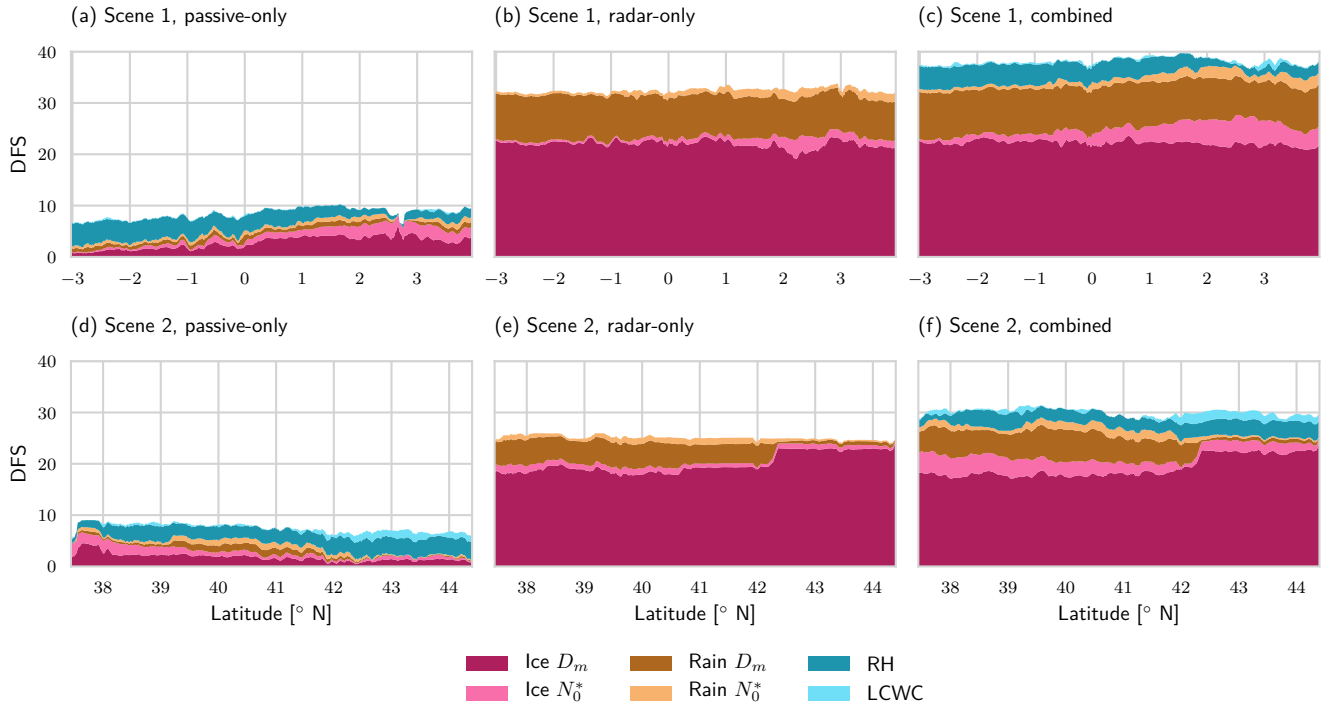
22

Figure 12. Degrees of freedom for signal for all retrieval configurations and both test scenes obtained with the Large Plate Aggregate model. The colored areas in each plot represent the contribution to the cumulative degrees of freedom from each retrieval quantity. Results for the first and second test scene are displayed in the first and second row, respectively. The first, second and third panel in each row show the results for the passive-only, radar-only and the combined retrieval.

between the fitted and true observations are observed. It is also in these regions, where the fits obtained with different particle models differ. These are both regions where the cloud is very thick and both the radar and passive observations are likely saturated. Since these are difficult regions for the retrieval it is not clear whether these differences can be related directly to the assumed particle shape. In contrast to this, the retrieval fits the observations well in the remaining parts of the scene. The exception is the GEM Graupel particle, for which quite significant misfits are observed in the first test scene between $0\,°$ N and $1\,°$ N latitude.

3.2.5 Humidity and cloud water

The developed passive and combined retrieval algorithms also retrieve profiles of RH and LCWC. For RH, both retrievals demonstrate sensitivity but no improvement was observed in the results of the combined retrieval compared to the passive-only retrieval.
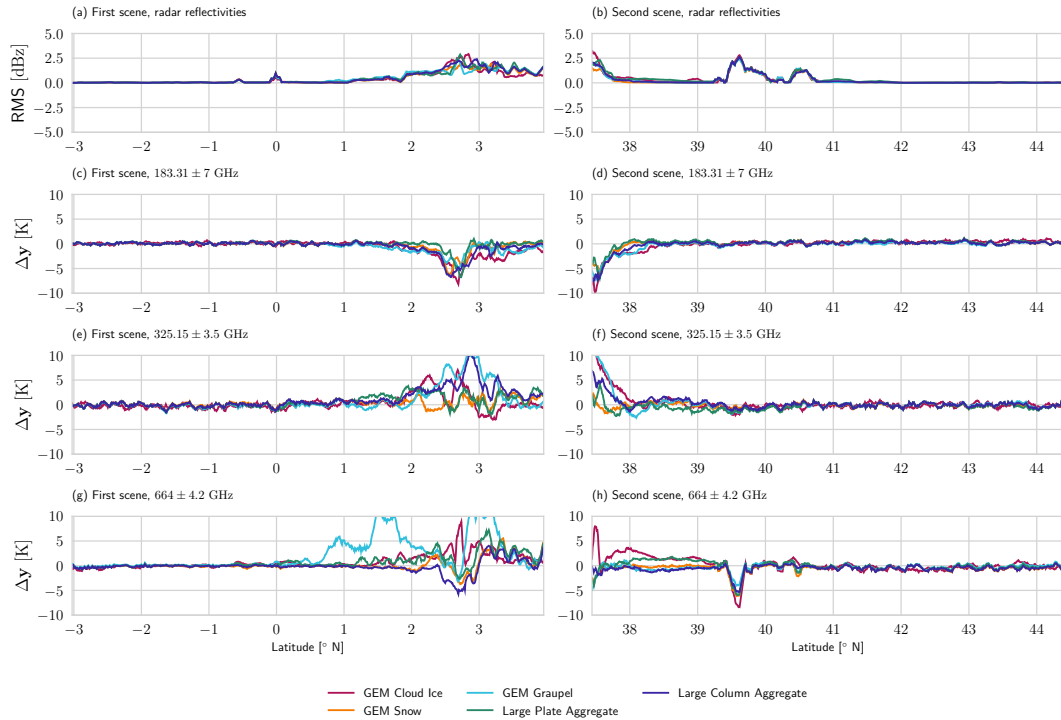
23

Figure 13. Residuals of the fitted observations. First row of panels shows the profile root mean squared error (RMS) between fitted ($\hat{\mathbf{y}}$) and true ($\mathbf{y}$) radar observations for the two test scenes. Rows 2, 3 and 4 show the residual $\Delta \mathbf{y} = \hat{\mathbf{y}} - \mathbf{y}$ for a selection of ICI channels.

Results of the LCWC retrieval are shown in Fig. 14. For the retrieved LCWC, the combined retrieval yields slightly improved
410   results compared to the passive-only retrieval. The improvements are observed mostly in the retrieved liquid cloud water path (LCWP) in the northern part of the scene. It should be noted that the cloud in this part is a mixed-phase cloud and that both retrievals successfully retrieve IWC and LCWC. At the center of the scene both retrievals fail to retrieve the LCWC. The reason for this is that in these regions rain is present, whose signal likely swamps any signal from the liquid cloud droplets.

4   Discussion

415   The principal aim of this study was to investigate the synergies between radar and passive sub-millimeter observations for the retrieval of frozen hydrometeors. To this end, a simplified numerical experiment has been presented, which demonstrates the existence of complementary information in the radar and passive microwave observations. Furthermore, a combined retrieval algorithm has been developed to demonstrate the feasibility of the synergistic retrieval and further explore their potential as well as current limitations.

420   The novelty of this work for lies, in part, in the application of ICI's sub-millimeter channels, which sets it apart from the combined retrievals developed for the TRMM and GPM missions. Moreover, the development of a fully consistent variational
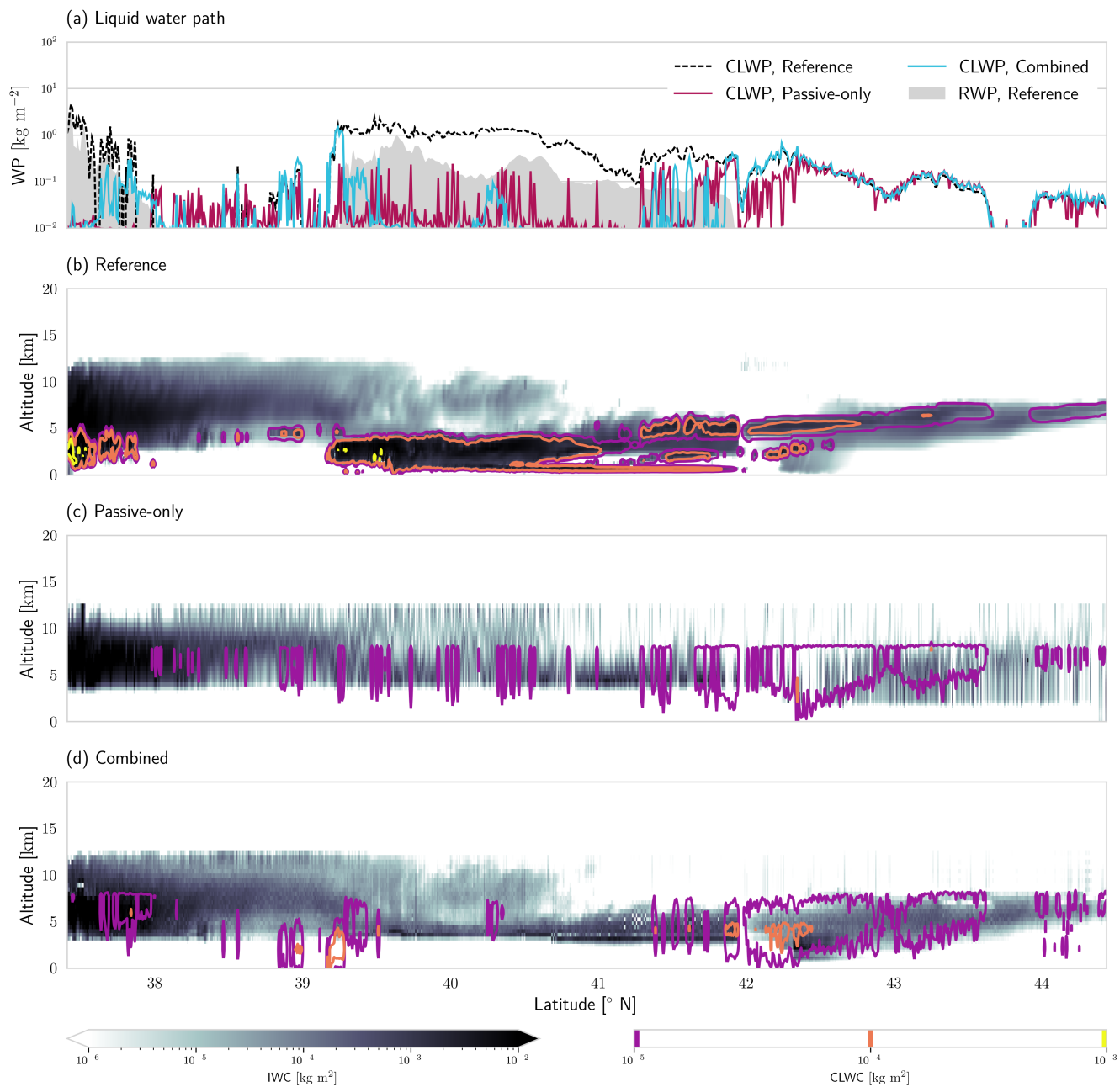
24

Figure 14. Reference and retrieved CLWC and IWC. Panel (a) shows the reference and retrieved LWP for each profile. Panel (b) displays reference LWC contours drawn on top of the total hydrometeor content. Retrieval results for passive-only and combined retrieval are given in Panel (c) and (d).

retrieval in which all retrieval quantities are retrieved simultaneously using the observations from all sensors is also novel. This allows comparison of the combined retrieval to equivalent radar-only and passive-only configurations and therefore a direct analysis of the synergies between the active and passive observations.

4.1 Fundamental synergies

The experiment presented in the first part of this study aimed to illustrate the fundamental synergies of active and passive microwave observations. It compared the cloud signals observed by a radar, a millimeter-wave radiometer and a sub-millimeter-wave radiometer. The results indicate that the combined observations can constrain the size and concentration of particles in the cloud. However, the complementary information content between the active and passive observations depends on both the properties of the observed cloud and the frequency of the observations. For the lower frequencies considered in this study, i.e. the highest frequency channels of the MWI radiometer, the regions where both observations provide complementary information on the particle size distribution of the cloud are limited to very high water content and particle sizes. It should be noted, however, that since the radar simulations neglect multiple scattering, these results may not fully carry over to space-borne observations. As the passive observing frequency increases, the regions of complementary information content extend down to smaller particle sizes and water content. Especially the highest-frequency channels of the ICI radiometer can therefore be expected to provide complementary information to a W-band radar in a combined observation scenario.

4.2 Combined cloud retrieval

In the second part of the study, we have presented results from a combined, variational cloud retrieval applied to synthetic observations from two test scenes from a CRM. The results of the combined retrieval were compared to that of a passive- and a radar-only version of the retrieval algorithm. The simulated observations assumed an airborne viewing geometry and therefore neglected potential errors caused by different or non-overlapping antenna beams as well as inhomogeneity of the atmosphere across the beams. A source of forward model error was included by applying a more complex microphysics scheme in the simulations than the one used in the retrieval. This permits assessment of the retrieval error caused by the simplified modeling of cloud microphysics in the retrieval.

4.2.1 Retrieval performance

Of the three considered retrieval implementations, the passive-only retrieval clearly performs worst in terms of retrieved IWC. It should be noted, however, that the passive-only retrieval presented here has not been fully optimized and should therefore not be taken as representative of the potential performance of the MWI and ICI radiometers for IWC retrievals. To ensure a fair comparison, the retrieval uses almost the same a priori assumptions as the other two retrievals, which in the presented case provide only very limited information on the vertical structure of the cloud. As has been shown also by other studies, the passive observations do provide information on the vertical distribution of ice in the atmospheric column (Wang et al., 2017; Grützun et al., 2018), but the information content is limited to a few degrees of freedom. It is therefore unlikely that the vertical

resolution of the passive-only retrieval can be improved drastically without further constraining it a priori, as it is typically done in retrievals that use Monte Carlo integration or neural networks (Pfreundschuh et al., 2018).

With respect to IWP, however, the passive retrieval can perform as well or even better than the radar-only retrieval. Furthermore, the results in Fig. 10 indicate that the passive observations provide some information on the particle number concentrations, which is not the case for the radar observations. This shows that passive observations at multiple frequencies can actually constrain the microphysics better than single-frequency radar-only observations alone although at a much lower vertical resolution.

As expected, the radar-only retrieval provides much better IWC retrievals than the passive-only version. However, the results of the two-moment retrieval exhibit systematic deviations from the reference values in certain regions of the cloud. The analysis shown in Fig. 8 and A2 reveals that these are caused by systematic errors in the retrieval of specific hydrometeor species from the GEM model. Interestingly, the 1M version of the radar-only retrieval did not produce the large errors in the second scene but produces systematic errors for the first test scene. This indicates that the a priori assumptions used in the retrieval do not provide a sufficiently good description of how the D_m and N_0^* parameters of the PSD co-vary and that the radar-only observations alone do not constrain both of them well enough. This is plausible also from an information content perspective since the radar provides only one piece of independent information at each range gate, which is insufficient to determine the two degrees of freedom (N_0^* and D_m) of the PSD. This hypothesis is confirmed by the radar-retrieved number concentration fields shown in Fig. 10 and Fig. 11. While the distribution of reference values has two modes corresponding to ice and snow, the retrieved values are nearly the same throughout the whole scene indicating that the observations themselves provide almost no information on particle concentrations.

Despite certain visible artifacts in the retrieved IWC field (Fig. 7), the combined retrieval yields the best overall performance for IWC and IWP as shown in Fig. 8 and Fig. 9 given that a suitable particle model is used. The benefit of the combined observations is even more pronounced in the retrieved number concentrations (Fig. 10). Here, the passive- and radar-only retrievals show little to no skill in retrieving the number concentrations. In contrast to this, the combined retrieval was able to reproduce the general structure of the number concentration field in regions where the cloud composition is homogeneous (Fig. 11). This shows that the combined retrieval is able to distinguish the microphysical properties of ice and snow in the test scenes. Instead of relying on the a priori, the combined retrieval can use information from the observations to constrain the cloud microphysics, which avoids the systematic errors observed in the radar-only retrievals.

The a priori assumptions used in this study were chosen similar to those of the DARDAR-CLOUD product since they represent well established and validated assumptions for ice cloud retrievals. The role of the a priori is to complement the observations with additional information required to make the retrieval problem tractable. For the hydrometeor retrieval this means that the a priori determines how information from the observations, which alone is insufficient to determine both degrees of freedom of the PSD, is distributed between its D_m and N_0^* parameters. For the radar-only retrieval, this works well for cloud systems containing both ice and snow but leads to biased retrievals of both IWC and IWP when this is not the case (Fig. 9). The DARDAR product uses co-located lidar observations to resolve the ambiguity where observations from both sensors are available. As our results show, this can be achieved also by combining a radar with passive microwave radiometers. However,

while the overlap between lidar and radar is restricted to relatively thin clouds, microwave radiometers can provide sensitivity even inside thick clouds.

4.2.2 Impact of the assumed particle shape

Our experiments show a stronger sensitivity to the assumed ice particle shape for the passive-only and the combined retrievals than the radar-only retrieval. The passive observations probe the particle at multiple frequencies and their sensitivity to particle shape, especially of the sub-millimeter channels, has been highlighted in several studies (Ekelund et al., 2020; Fox et al., 2019).

Only the combined retrieval was able to yield accurate IWC retrievals for both test scenes for suitable choices of the particle model. However, if an unsuitable particle shape is chosen, the induced errors may actually outweigh the benefits of the combined retrieval as is the case for the Large Column Aggregate and the GEM Cloud Ice shapes (Fig. 9). Judging from the particle properties displayed in Fig. 4, a likely explanation for the good performance of the Large Plate Aggregate and the GEM Graupel particle is that their properties are intermediate to those of GEM Cloud Ice and GEM Snow, which are the dominating shapes in the test scenes. For the test scenes considered here, this means that accurate IWC retrievals can be achieved using only a single hydrometeor species with suitable scattering properties which are intermediate to snowflakes and heavily rimed particles. This is in agreement with Ekelund et al. (2020) who found the Large Plate Aggregate to yield good agreement with observations from the GPM Microwave Imager at 183.31 ± 7 GHz.

The analysis of the residuals of the retrieval fit (Fig. 13) showed that the residuals for different particle shapes differ most where the cloud is thick. Differences between different particles are observed, but no relationship to the retrieval accuracy in terms of IWC can be established. The GEM Graupel particle, for example, yields accurate IWC retrievals but gives the worst fit for the first test scene. A likely explanation for this is that the retrieved IWC depends mostly on the efficiency with respect to water content of the interaction between the particle and the radiation, whereas the retrieval residual is likely due to the relative efficiencies at different frequencies. Moreover, in the remaining parts of the scenes, there are no differences in the residuals for different particles. This means that the retrieval can fit the observations well regardless of the assumed particle shape and indicates that the observations alone do not strongly constrain the particle shape. This makes it unlikely that particle shape can be retrieved from observations, thus requiring it to be determined a priori.

It should be noted, that none of the presented retrievals accounts for the error caused by the simplified forward model and the choice of the particle model. This has not been pursued here because of the difficulty of fitting a suitable error model to these errors, which are likely non-Gaussian and scene-dependent. However, it is likely that accounting for them can improve retrieval performance and weaken the impact of the particle choice on the retrieval results.

4.2.3 Humidity and cloud water

As an outlook, results from the LCWC retrieval have been provided despite it not being a focus of this study. Fig. 14 shows improvements in retrieved LCWP and LCWC in the results of the combined retrieval compared to the passive-only retrieval. Although also the passive-only retrieval shows sensitivity to LCWC, the results are less robust than those of the combined retrieval. This shows that combined millimeter and sub-millimeter radiometers, in particular in combination with radar ob-

servations, can be used for retrieving both frozen and liquid cloud water content in mixed-phase clouds. This conclusion is supported by the information content analysis in Fig. 12, which shows that the passive observations provide some information on LCWC and that this is increased slightly for the combined retrieval.

For the water vapor retrieval, no significant improvements in the combined retrieval results were observed and also the analysis of the information content does not show any increase in information content. This indicates that the combined observations do not provide any direct synergies for the retrieval of humidity.

4.2.4 Limitations

An important limitation of this study is its scope: The aim here was not to develop a production-ready combined retrieval product but rather a proof-of-concept to explore this observational approach. The retrieval results presented here should therefore not be interpreted in absolute terms. The primary results are based on the relative performances of the three retrieval methods: Given equivalent a priori assumptions, the combined retrieval demonstrates higher sensitivity to the microphysical properties than the radar-only retrieval and lower errors in terms of IWC than the passive-only retrieval.

Moreover, this study is purely based on simulations and restricted to two selected model test scenes. The validity of the presented results thus depends on how well cloud microphysics are represented in the GEM model. While this may affect interpretation of the results in absolute terms, the main findings of this work, which are based on a relative comparison of the retrieval results, should be less dependent on the realism of the test scenes.

As has been stated above, simulated observations used in this study assumed a viewing geometry that is realistic only for airborne observations. They therefore do not provide a realistic assessment of the potential of a space-borne satellite mission involving ICI, MWI and a W-band radar. For this it would be necessary to take into account a more realistic viewing geometry, beam-filling errors as well as multiple scattering in the radar observations. Quantifying the effect of these error sources on the retrieval synergies is left for future investigation.

5 Conclusions

The main conclusion from this work is that the combination of radar and sub-millimeter radiometer observations can, to some extent, constrain both the size and number concentration of frozen hydrometeors (Fig. 5). The increased sensitivity of the combined observations to the microphysical properties of hydrometeors helps to improve the accuracy of IWC retrievals and avoid systematic errors observed in an equivalent radar-only retrieval (Fig. 8, 9). Moreover, the combined retrieval showed clear sensitivity to particle number concentrations and was able reproduce their vertical structure in regions where the cloud composition is homogeneous (Fig. 10, 11).

The results particularly highlight the importance of sub-millimeter observations for combined retrievals of frozen hydrometeors. While observations at currently available microwave frequencies provide information complementary to that from a radar only for thick clouds with very large particles ($D_m > 800\,\mu\mathrm{m}, \mathrm{IWC} > 10^{-4}\,\mathrm{kg\,m^{-3}}$), frequencies above 200 GHz pro-

vide additional information on cloud microphysics (Fig. 5) at smaller particles sizes and water content ($D_m > 200\,\mu\mathrm{m}$, $\mathrm{IWC} > 10^{-5}\ \mathrm{kg\ m}^{-3}$).

Regarding the representation of hydrometeors in the retrieval, our results indicate that complex mixes of hydrometeors can
555 be accurately represented using a single, suitable habit mix. In particular, our results indicate that a suitable habit should have scattering properties that are intermediate between strongly rimed and more snow-flake like particles (Fig. 4, 9).

A direct application of the synergistic retrieval algorithm developed in this study are flight campaigns involving the International Sub-millimetre Airborne Radiometer (ISMAR, Fox et al. (2017)) combined for example with a radar on another aircraft or the Microwave Radar/radiometer for Arctic Clouds (MiRAC, Mech et al. (2019)). The ability of the combined retrieval to
560 constrain two moments of the PSD of frozen hydrometeors should make it a valuable tool for validating the representation of clouds in cloud-resolving or large-eddy simulations which typically employ two-moment schemes. Moreover, since our results indicate retrieval skill also for LCWC in mixed-phase clouds, such observations can be used to study the properties of these clouds which play an important role for the climate of the arctic. The sensitivity to LCWC of the passive observations is also a promising indication for combined ICI/MWI retrievals.

565 Ultimately, spaceborne combined radar and sub-millimeter observations can be a way forward towards reducing the large uncertainties in the observational record of ice hydrometeors. The Metop program provides an opportunity for a synergistic radar mission involving the MWI and ICI radiometers. Alternatively, the combination could be realized also by a dedicated small mission, such as the Earth's NexT-generation ICE mission (ENTICE) described in Jiang et al. (2019). The results presented here clearly show the potential this approach and can provide a first step towards the development of a retrieval algorithm
570 for a space-borne configuration. This, however, will require extending the algorithm to the more complex viewing geometry. Moreover, to quantify the potential benefits of such a mission additional studies will be required to analyze the additional error sources which affect spaceborne observations.

Code availability. All code used to produce the results in this study is available from a public repository (Simon Pfreundschuh, 2019).

Data availability. Data to reproduce the simulations leading to the presented results will be made available on request.

Appendix A: Results from second test scene

The retrieved IWC obtained using the Large Plate Aggregate for the second scene is shown in Fig. A1. Just as the first scene, this test scene contains a region in the south where the final OEM cost, shown in Panel (a), is increased for the passive-only and combined retrievals. This is again a region of very dense cloud consisting of graupel and snow. Qualitatively, the results of the IWC retrieval are very similar to those from the first scene. While the passive-only retrieval provides only very low vertical resolution, both the radar-only and combined retrieval reproduce the vertical structure of the cloud well. The radar-only retrieval consistently overestimates the IWC in the scene, which is not the case for the combined retrieval.

Scatter plots for the retrieval results from the second scene are shown in Fig. A2. Except for the lack of cloud ice in the scene, the results are similar to what has been observed in the first scene: The radar-only retrieval exhibits the same systematic error for the retrieval of snow as in the first scene. Again, this is corrected by the combined retrieval for most of the tested particle shapes. The exception are the GEM Cloud Ice and the Large Column Aggregate particles for which the retrieval does not perform as well.
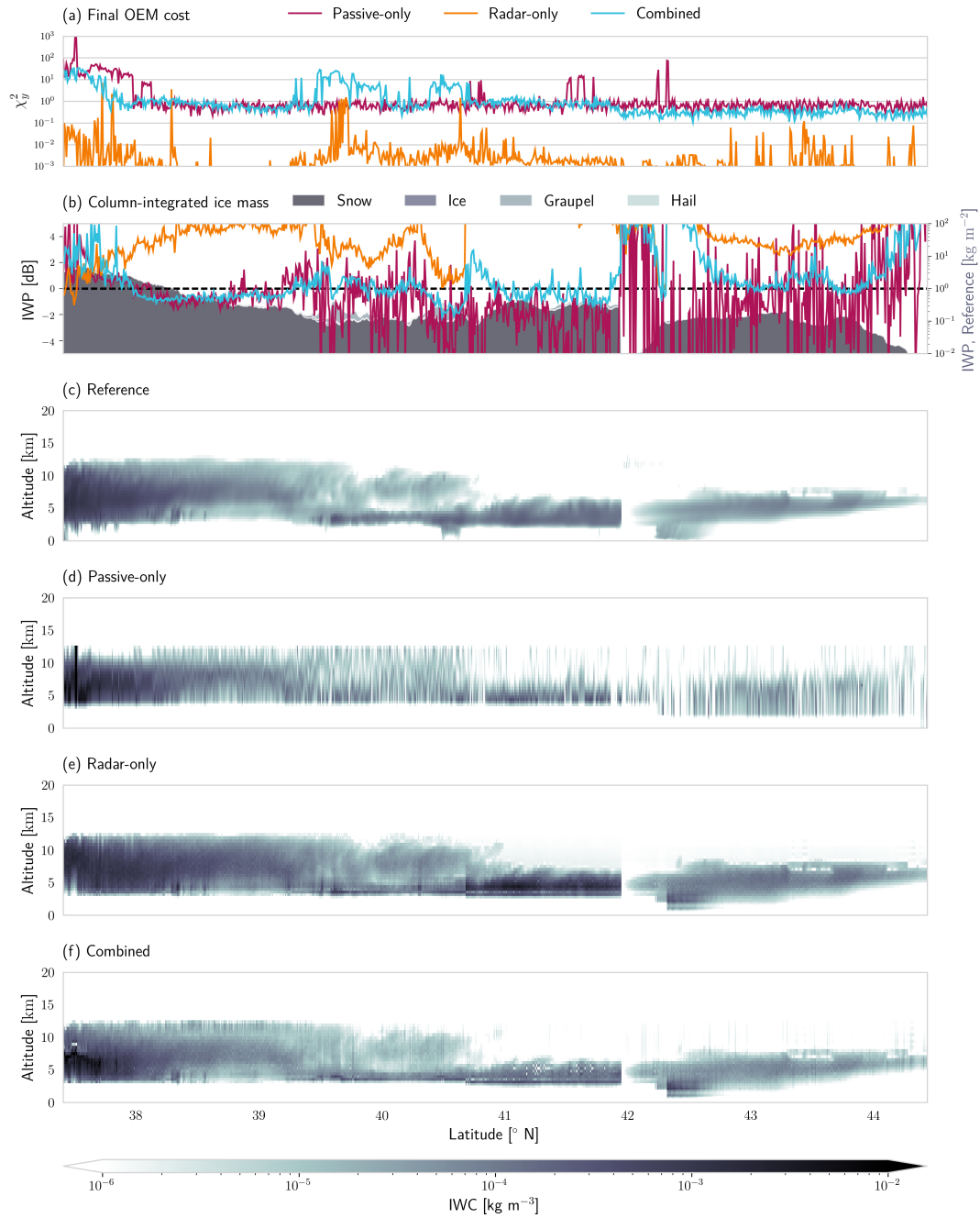
Figure A1. Results of the ice hydrometeor retrieval for the second test scene. Panel (a) displays the value of the χ_y^2 diagnostic normalized by the dimension of the measurement space of the corresponding retrieval. Panel (b) shows retrieved IWP in dB relative to the reference IWP. Reference IWP and the contributions from different hydrometeor classes are displayed by the filled areas in the background. Panel (c) displays the reference mass concentrations from the model scene. Panel (d), (e) and (f) display the retrieval results for the passive-only, radar-only and combined retrieval, respectively.
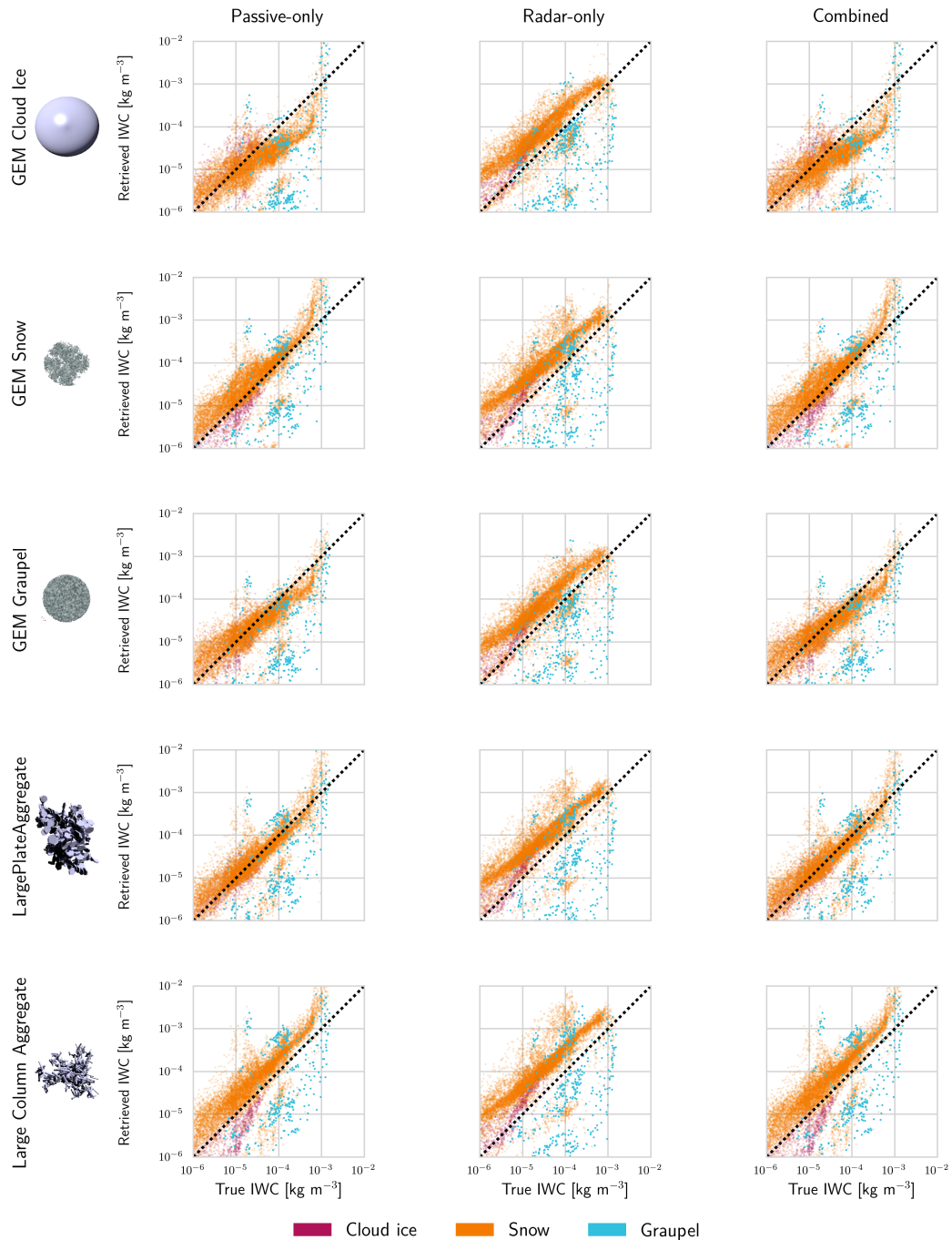
Figure A2. Scatter plots of the reference and retrieved IWC for the second test scene. The rows show the retrieval results for a given assumed ice particle model. The first column of each row displays a rendering of the particle model. The following rows display the results for the passive-only, the radar-only and the combined retrieval.

590

595

600

References

Aires, F., Prigent, C., Buehler, S. A., Eriksson, P., Milz, M., and Crewell, S.: Towards more realistic hypotheses for the information content analysis of cloudy/precipitating situations – Application to a hyperspectral instrument in the microwave, Q. J. R. Meteorol. Soc., 145, 1–14, https://doi.org/10.1002/qj.3315, 2019.

Birman, C., Mahfouf, J.-F., Milz, M., Mendrok, J., Buehler, S. A., and Brath, M.: Information content on hydrometeors from millimeter and sub-millimeter wavelengths, Tellus, 69, 1271 562, https://doi.org/10.1080/16000870.2016.1271562, 2017.

Bony, S., Stevens, B., Frierson, D. M., Jakob, C., Kageyama, M., Pincus, R., Shepherd, T. G., Sherwood, S. C., Siebesma, A. P., Sobel, A. H., et al.: Clouds, circulation and climate sensitivity, Nat. Geosci., 8, 261, https://doi.org/10.1038/ngeo2398, 2015.

Boucher, O., Randall, D., Artaxo, P., Bretherton, C., Feingold, G., Forster, P., Kerminen, V.-M., Kondo, Y., Liao, H., Lohmann, U., Rasch, P., Satheesh, S., Sherwood, S., Stevens, B., and Zhang, X.: Clouds and Aerosols, book section 7, p. 571–658, Cambridge University Press, Cambridge, United Kingdom and New York, NY, USA, https://doi.org/10.1017/CBO9781107415324.016, 2013.

Brath, M., Fox, S., Eriksson, P., Harlow, R. C., Burgdorf, M., and Buehler, S. A.: Retrieval of an ice water path over the ocean from ISMAR and MARSS millimeter and submillimeter brightness temperatures, Atmos. Meas. Tech., 11, 611–632, https://doi.org/10.5194/amt-11-611-2018, 2018.

Buehler, S. A., Mendrok, J., Eriksson, P., Perrin, A., Larsson, R., and Lemke, O.: ARTS, the Atmospheric Radiative Transfer Simulator – version 2.2, the planetary toolbox edition, Geosci. Model Dev., 11, 1537–1556, https://doi.org/10.5194/gmd-11-1537-2018, 2018.

Cazenave, Q., Ceccaldi, M., Delanoë, J., Pelon, J., Groß, S., and Heymsfield, A.: Evolution of DARDAR-CLOUD ice cloud retrievals: new parameters and impacts on the retrieved microphysical properties, Atmos. Meas. Tech., 12, 2819–2835, https://doi.org/10.5194/amt-12-2819-2019, 2019.

Côté, J., Gravel, S., Méthot, A., Patoine, A., Roch, M., and Staniforth, A.: The operational CMC–MRB global environmental multi-scale (GEM) model. Part I: Design considerations and formulation, Mon. Weather Rev., 126, 1373–1395, https://doi.org/10.1175/1520-0493(1998)126<1373:TOCMGE>2.0.CO;2, 1998.

Delanoë, J., Protat, A., Testud, J., Bouniol, D., Heymsfield, A. J., Bansemer, A., Brown, P., and Forbes, R.: Statistical properties of the normalized ice particle size distribution, J. Geophys. Res.-Atmos., 110, https://doi.org/10.1029/2004JD005405, 2005.

Delanoë, J., Heymsfield, A. Protat, A., Bansemer, A., and Hogan, R.: Normalized particle size distribution for remote sensing application, J. Geophys. Res.-Atmos., 119, 4204–4227, https://doi.org/10.1002/2013JD020700, 2014.

Duncan, D. I. and Eriksson, P.: An update on global atmospheric ice estimates from satellite observations and reanalyses, Atmos. Chem. Phys., 18, 11 205, https://doi.org/10.5194/acp-18-11205-2018, 2018.

Ekelund, R., Eriksson, P., and Pfreundschuh, S.: Using passive and active observations at microwave and sub-millimetre wavelengths to constrain ice particle models, Atmos. Meas. Tech., 13, 501–520, https://doi.org/10.5194/amt-13-501-2020, 2020.

Eliasson, S., Buehler, S. A., Milz, M., Eriksson, P., and John, V. O.: Assessing observed and modelled spatial distributions of ice water path using satellite data, Atmos. Chem. Phys., 11, 375–391, https://doi.org/10.5194/acp-11-375-2011, 2011.

Eriksson, P., Ekelund, R., Mendrok, J., Brath, M., Lemke, O., and Buehler, S. A.: A general database of hydrometeor single scattering properties at microwave and sub-millimetre wavelengths, Earth Syst. Sci. Data, 10, 1301–1326, https://doi.org/10.5194/essd-10-1301-2018, 2018.

Eriksson, P., Rydberg, B., Mattioli, V., Thoss, A., Accadia, C., Klein, U., and Buehler, S. A.: Towards an operational Ice Cloud Imager (ICI) retrieval product, Atmos. Meas. Tech., 13, 53–71, https://doi.org/10.5194/amt-13-53-2020, 2020.

Evans, K. F., Wang, J. R., Racette, P. E., Heymsfield, G., and Li, L.: Ice Cloud Retrievals and Analysis with the Compact Scanning Submillimeter Imaging Radiometer and the Cloud Radar System during CRYSTAL FACE, J. Appl. Meteorol., 44, 839–859, https://doi.org/10.1175/JAM2250.1, 2005.

645 Fox, S., Lee, C., Moyna, B., Philipp, M., Rule, I., Rogers, S., King, R., Oldfield, M., Rea, S., Henry, M., Wang, H., and Harlow, R. C.: ISMAR: an airborne submillimetre radiometer, Atmos. Meas. Tech., 10, 477–490, https://doi.org/10.5194/amt-10-477-2017, 2017.

Fox, S., Mendrok, J., Eriksson, P., Ekelund, R., O'Shea, S. J., Bower, K. N., Baran, A. J., Harlow, R. C., and Pickering, J. C.: Airborne validation of radiative transfer modelling of ice clouds at millimetre and sub-millimetre wavelengths, Atmos. Meas. Tech., 12, 1599–1617, https://doi.org/10.5194/amt-12-1599-2019, 2019.

650 Geer, A. J., Baordo, F., Bormann, N., Chambon, P., English, S. J., Kazumori, M., Lawrence, H., Lean, P., Lonitz, K., and Lupu, C.: The growing impact of satellite observations sensitive to humidity, cloud and precipitation, Q. J. R. Meteorol. Soc., 143, 3189–3206, https://doi.org/10.1002/qj.3172, 2017.

Grecu, M., Olson, W. S., and Anagnostou, E. N.: Retrieval of Precipitation Profiles from Multiresolution, Multifrequency Active and Passive Microwave Observations, Journal of Applied Meteorology, 43, 562–575, https://doi.org/10.1175/1520-0450(2004)043<0562:ROPPFM>2.0.CO;2, 2004.

655

Grecu, M., Olson, W. S., Munchak, S. J., Ringerud, S., Liao, L., Haddad, Z., Kelley, B. L., and McLaughlin, S. F.: The GPM Combined Algorithm, J. Atmos. Oceanic Technol., 33, 2225–2245, https://doi.org/10.1175/JTECH-D-16-0019.1, 2016.

Grützun, V., Buehler, S. A., Kluft, L., Mendrok, J., Brath, M., and Eriksson, P.: All-sky information content analysis for novel passive microwave instruments in the range from 23.8 to 874.4 GHz, Atmos. Meas. Tech., 11, 4217–4237, https://doi.org/10.5194/amt-11-4217-2018, 2018.

660

Hou, A. Y., Kakar, R. K., Neeck, S., Azarbarzin, A. A., Kummerow, C. D., Kojima, M., Oki, R., Nakamura, K., and Iguchi, T.: The Global Precipitation Measurement Mission, Bull. Amer. Met. Soc., 95, 701–722, https://doi.org/10.1175/BAMS-D-13-00164.1, 2014.

Hunter, J. D.: Matplotlib: A 2D graphics environment, Comput. Sce. Eng., 9, 90–95, https://doi.org/10.1109/MCSE.2007.55, 2007.

Jiang, J. H., Yue, Q., Su, H., Kangaslahti, P., Lebsock, M., Reising, S., Schoeberl, M., Wu, L., and Herman, R. L.: Simulation of Remote Sensing of Clouds and Humidity From Space Using a Combined Platform of Radar and Multifrequency Microwave Radiometers, Earth Space. Sci., 6, 1234–1243, https://doi.org/10.1029/2019EA000580, 2019.

665

Jiménez, C., Buehler, S., Rydberg, B., Eriksson, P., and Evans, K.: Performance simulations for a submillimetre-wave satellite instrument to measure cloud ice, Q. J. R. Meteorol. Soc., 133, 129–149, https://doi.org/10.1002/qj.134, 2007.

Kummerow, C., Barnes, W., Kozu, T., Shiue, J., and Simpson, J.: The tropical rainfall measuring mission (TRMM) sensor package, Journal of atmospheric and oceanic technology, 15, 809–817, 1998.

670

Kummerow, C. D., Randel, D. L., Kulie, M., Wang, N.-Y., Ferraro, R., Munchak, J. S., and Petkovic, V.: The Evolution of the Goddard Profiling Algorithm to a Fully Parametric Scheme, J. Atmos. Oceanic Technol., 32, 2265–2280, https://doi.org/10.1175/JTECH-D-15-0039.1, 2015.

Liebe, H. J., Hufford, G. A., and Cotton, M. G.: Propagation modeling of moist air and suspended water/ice particles at frequencies below

675 1000 GHz, in: AGARD conference proceedings 542: Atmospheric propagation effects through natural and man-made obscurants for visible to mm-wave radiation, pp. 3.1–3.10, Palma de Mallorca, Spain, 17–20 May 1993, 1993.

Mech, M., Kliesch, L.-L., Anhäuser, A., Rose, T., Kollias, P., and Crewell, S.: Microwave Radar/radiometer for Arctic Clouds (MiRAC): first insights from the ACLOUD campaign, Atmospheric Measurement Techniques, 12, 5019–5037, https://doi.org/10.5194/amt-12-5019-2019, 2019.

680 Milbrandt, J. A. and Yau, M. K.: A multimoment bulk microphysics parameterization. Part II: A proposed three-moment closure and scheme description, J. Atmos. Sci., 62, 3065–3081, https://doi.org/10.1175/JAS3534.1, 2005.

Munchak, S. J. and Kummerow, C. D.: A Modular Optimal Estimation Method for Combined Radar–Radiometer Precipitation Profiling, J. Atmos. Oceanic Technol., 50, 433–448, https://doi.org/10.1175/2010JAMC2535.1, 2011.

Perez, F. and Granger, B. E.: IPython: A System for Interactive Scientific Computing, Computing in Science Engineering, 9, 21–29, 685 https://doi.org/10.1109/MCSE.2007.53, 2007.

Pfreundschuh, S., Eriksson, P., Duncan, D., Rydberg, B., Håkansson, N., and Thoss, A.: A neural network approach to estimating a posteriori distributions of Bayesian retrieval problems, Atmos. Meas. Tech., 11, 4627–4643, https://doi.org/10.5194/amt-11-4627-2018, 2018.

Prigent, C., Aires, F., Wang, D., Fox, S., and Harlow, C.: Sea-surface emissivity parametrization from microwaves to millimetre waves, Q. J. R. Meteorol. Soc., 143, 596–605, https://doi.org/10.1002/qj.2953, 2017.

690 Rodgers, C. D.: Inverse methods for atmospheric sounding: theory and practice, vol. 2, World scientific, https://doi.org/10.1142/3171, 2000.

Rosenkranz, P. W.: Absorption of microwaves by atmospheric gases, in: Atmospheric remote sensing by microwave radiometry, edited by Janssen, M. A., pp. 37–90, John Wiley and Sons, Inc., New York, USA, 1993.

Rosenkranz, P. W.: Water vapor microwave continuum absorption: A comparison of measurements and models, Radio Sci., 33, 919–928, https://doi.org/10.1029/98RS01182, 1998.

695 Simon Pfreundschuh: mcrf – A microwave cloud retrieval framework, https://doi.org/10.5281/zenodo.3467316, 2019.

Stamnes, K., Tsay, S.-C., Wiscombe, W., and Laszlo, I.: DISORT, a general-purpose Fortran program for discrete-ordinate-method radiative transfer in scattering and emitting layered media: documentation of methodology, Tech. rep., Tech. rep., Dept. of Physics and Engineering Physics, Stevens Institute of . . . , 2000.

Stephens, G. L., Vane, D. G., Boain, R. J., Mace, G. G., Sassen, K., Wang, Z., Illingworth, A. J., O'connor, E. J., Rossow, W. B., Durden, 700 S. L., Miller, S. D., Austin, R. T., Benedetti, A., and Mitrescu, C. a.: THE CLOUDSAT MISSION AND THE A-TRAIN, Bull. Amer. Met. Soc., 83, 1771–1790, https://doi.org/10.1175/BAMS-83-12-1771, 2002.

Tanelli, S., Durden, S. L., Im, E., Pak, K. S., Reinke, D. G., Partain, P., Haynes, J. M., and Marchand, R. T.: CloudSat's Cloud Profiling Radar After Two Years in Orbit: Performance, Calibration, and Processing, IEEE T. Geosci. Remote, 46, 3560–3573, https://doi.org/10.1109/TGRS.2008.2002030, 2008.

705 The Python Language Foundation: The Python Language Reference, https://docs.python.org/3/reference/index.html, 2018.

van der Walt, S., Colbert, S. C., and Varoquaux, G.: The NumPy Array: A Structure for Efficient Numerical Computation, Computing in Science Engineering, 13, 22–30, https://doi.org/10.1109/MCSE.2011.37, 2011.

Waliser, D. E., Li, J.-L. F., Woods, C. P., Austin, R. T., Bacmeister, J., Chern, J., Del Genio, A., Jiang, J. H., Kuang, Z., Meng, H., Minnis, P., Platnick, S., Rossow, W. B., Stephens, G. L., Sun-Mack, S., Tao, W.-K., Tompkins, A. M., Vane, D. G., Walker, C., and Wu, D.: Cloud ice: 710 A climate model challenge with signs and expectations of progress, J. Geophys. Res.-Atmos., 114, https://doi.org/10.1029/2008JD010015, 2009.

Wang, D., Prigent, C., Aires, F., and Jimenez, C.: A Statistical Retrieval of Cloud Parameters for the Millimeter Wave Ice Cloud Imager on Board MetOp-SG, IEEE Access, 5, 4057–4076, https://doi.org/10.1109/ACCESS.2016.2625742, 2017.

Xie, X., Crewell, S., Löhnert, U., Simmer, C., and Miao, J.: Polarization signatures and brightness temperatures caused by horizontally 715 oriented snow particles at microwave bands: Effects of atmospheric absorption, Journal of Geophysical Research: Atmospheres, 120, 6145–6160, 2015.